J. Mech. Phys. Solids 188 (2024) 105661

Contents lists available at ScienceDirect

Journal of the Mechanics and Physics of Solids

journal homepage: www.elsevier.com/locate/jmps

Mechanics of abrasion-induced particulate matter emission

Ketian Li [1], Yanchu Zhang [1], Kunhao Yu, Haixu Du, Constantinos Sioutas [*], Qiming Wang [*]

Sonny Astani Department of Civil and Environmental Engineering, University of Southern California, Los Angeles, CA 90089, United States

ARTICLE INFO

Keywords:
Abrasion mechanics
Fracture mechanics
Fatigue fracture
Particulate matter
Marine microplastics

ABSTRACT

Microplastic pollution constitutes a substantially detrimental type of environmental contamination and poses threats to human health. Among the sources of airborne and marine microplastics, evidence indicates that non-exhaust emissions resulting from tire abrasion and other organic materials have emerged as a notable contributor. However, the mechanistic understanding of abrasion emission of organic materials has remained elusive. To fill the gap, we here develop a multi-scale abrasion mechanics model using the principles of linear elastic fracture mechanics. Macroscopically, material wear and tear can be viewed as a process of macro-crack propagation associated with the fatigue fracture. Microscopically, we consider the effect of microcracks propagating under cyclic loading on the material modulus and energy release rate during fatigue fracture. This framework leads to an evaluation of the effective energy release rate for the abrasion-induced emission of particulate matter, thus leading to a calculation of the concentration of the emitted particulate matter with varied sizes. The theory is validated by corresponding experiments and high consistency is exhibited between the theoretical and experimental results. This research constructs a quantitative relationship between fracture mechanics and abrasion emissions. This research not only paves the way for a mechanistic understanding of particulate matter pollution from a solid mechanics perspective but also offers rational guidance for modern society to alleviate airborne particulate matter and marine microplastic abrasion emissions.

1. Introduction

The prevalence of microplastic pollution has been widely studied and represents a significantly harmful form of environmental contamination (Carpenter et al., 1972; Cole et al., 2011; Hidalgo-Ruz et al., 2012). After the generation of microplastic particles through various human activities, those with diameters less than 10 micrometers tend to remain suspended in the air for extended periods, contributing to air pollution (Evangeliou et al., 2020), while others tend to deposit in the freshwater ecosystem from which a substantial proportion of microplastics are transported over great distances and eventually deposited in oceans (Browne et al., 2011; Cole et al., 2011). Microplastic particles suspended in the air pose a strong threat to human health (Brunekreef and Holgate, 2002; Buckeridge et al., 2002; Fan et al., 2006). Fine particles can enter the human respiratory system and even the cardiovascular system to cause severe diseases and shorten human lifespan (Fan et al., 2006; Kampa and Castanas, 2008; Masiol et al., 2012). Microplastic particles deposited on freshwater ecosystems or deposited in the ocean will greatly damage the ecological environment (Cole et al.,

* Corresponding authors.
E-mail addresses: sioutas@usc.edu (C. Sioutas), qimingw@usc.edu (Q. Wang).
[1] These authors contributed equally to this work.

https://doi.org/10.1016/j.jmps.2024.105661
Received 18 January 2024; Received in revised form 26 March 2024; Accepted 24 April 2024
Available online 25 April 2024

2013; Ivar do Sul and Costa, 2014), and even endanger human health again through Bioaccumulation (Andrady, 2011; Besseling et al., 2013; Boerger et al., 2010). Due to the difficulty of recycling microplastics, reducing the generation of microplastics from the source has become the focus of attention. Studies have shown that as exhaust emissions of particulate matter have been significantly reduced by tight regulations, traffic-related non-exhaust emissions, such as tire wear (Fig. 1a) and brake wear have become the major source of airborne particulate matter in urban society (Fig. 1b) (Kole et al., 2017; Penkała et al., 2018; Sommer et al., 2018; Thorpe and Harrison, 2008; Wagner et al., 2018). Evidence showed that the tire wear emits significant amounts of microplastic particles over their lifetime (approximately 40,000 to 50,000 km), with about 10 %−50 % of the tire weight worn and discharged into the environment (Fig. 1c), equating to 0.8 kg/year per capita globally (Evangeliou et al., 2020; Parker-Jurd et al., 2021). The significance of this becomes clear when considering the global vehicle amount, which is estimated to exceed 1 billion currently and predicted to exceed 2 billion by 2040. Particles emitted from brake wear also reached 500,000 tons per year and are expected to continually increase (Parker-Jurd et al., 2021). The development of efficient methods for reducing emissions from tire and organic material abrasion is highly desired for modern society. However, without a thorough understanding of the underlying mechanisms of abrasion emissions, any indiscriminately proposed strategy may lack a rational basis.

To unveil the mechanism of abrasion emissions from tires and other organic materials, previous studies have primarily focused on the experimental characterization of particulate matter produced through abrasion (Wagner et al., 2018), both in the laboratory (Cadle et al., 1979; Tonegawa and Sasaki, 2021) and in field conditions (Harrison et al., 2012; Pant and Harrison, 2013; Parker-Jurd et al., 2021). Despite extensive experiments have been carried out in the laboratory and the field, the particle size distribution and physical and chemical properties of the released particles have been unexplored, and the mechanism of the abrasive emission of such organic materials is still elusive to date (Panko et al., 2018; Penkała et al., 2018; Thorpe and Harrison, 2008). Some scholars postulated that the microplastic generation is related to the thermally induced shedding of organic materials (Penkała et al., 2018; Thorpe and Harrison, 2008). However, this postulation remained a matter of speculation. Currently, no theoretical model has been established and there is a lack of robust data and empirical evidence to support the above postulation (Penkała et al., 2018; Thorpe and Harrison, 2008). Other researchers believed that abrasion should be considered a mechanics problem linked to material fracture (Akono et al., 2011; Akono and Ulm, 2011, 2012, 2014; Archard, 1953; Champ et al., 1974; Suh, 1973). Their models can explain the mechanism of abrasion fracture but cannot link the abrasion fracture to the concentration and size distribution of the emitted particulate matter. A mechanistic understanding framework urgently needs to be established to construct the linkage between abrasion fracture and particulate emission. Such a mechanistic model is expected to provide rational and quantitative guidance for mitigating the abrasion emissions of airborne particulate matter and marine microplastics.

In this study, we developed a multi-scale theoretical framework to understand the organic material abrasion process and the generation of micro-particles, thus establishing a quantitative connection between organic material abrasion emission and material mechanical properties. Two main processes take place simultaneously for organic materials to be scratched off by hard objects. On the macro level, we believed that organic materials would form macroscopic cracks on the scratched surface as the hard object cuts and

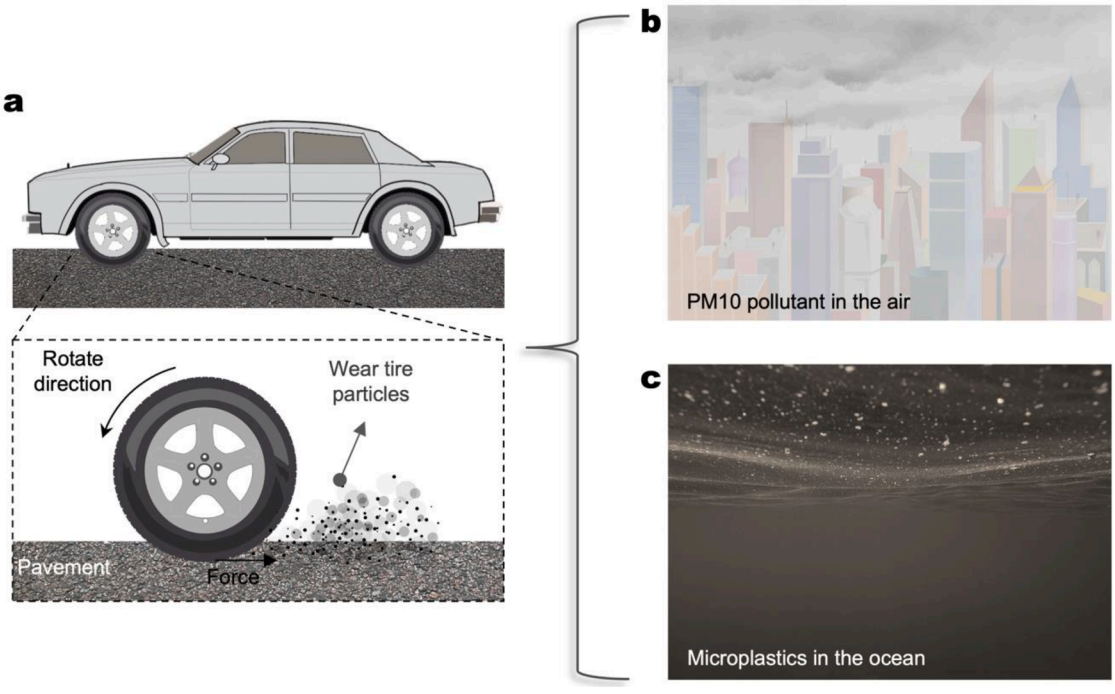

Fig. 1. Overall impact of abrasion emission of tire particles. (a) Schematics to illustrate the abrasion emission of tire particles. (b) Airborne PM10 pollutant. (c) Microplastics in the ocean.

scoops the organic material. This macrocrack will then propagate under cyclic loading and become the primary cause of material detachment. On the micro level, organic materials can be considered as cracked bodies containing micro-cracks that propagate under cyclic loads. These micro-cracks affect the material mechanical properties and lead to the formation of micro-particles during the material detachment. Both macroscopic and microscopic crack propagation result from fatigue behavior and are regulated by two energy release rates. On this basis, a theoretical framework was established, enabling the calculation of the concentration of the emitted particulate matter with varied sizes. Our theoretical framework was applied to five organic materials with varying mechanical properties, demonstrating a high degree of concordance with experimental data. This framework quantitatively relates the organic material wear emission to material mechanical properties. For the first time, the proposed model explains the mechanism for particulate matter emissions from organic material wear. This framework potentially provides guidance for reducing air particulate and oceanic microplastic generated from abrasion emissions.

The plan of this paper is as follows: In Section 2, the experimental methods and results of the abrasion-induced particle matter emission of organic material are presented. In Section 3, we establish a theoretical framework to explain the fatigue fracture behavior of macroscopic cracks, the effect of microscopic cracks on material properties, and the energy release rate of microscopic cracks. Subsequently, we constructed a model that can calculate the concentration of emitted particles with varied sizes. In Section 4, we present the theoretically calculated results of models and illustrate the comparison between the theoretical and experimental results. The conclusive remarks are given in Section 5.

2. Experimental

We selected polyurethane elastomers as the experimental organic materials for abrasion testing, because the fracture toughness of these materials could be easily tuned by varying the molar mass of the backbone molecule.

Poly(tetrahydrofuran) (PolyTHF, average molar mass 250, 650, 1000, 2000 g/mol), isophorone diisocyanate (IPDI), Ethyl acetate, and dibutyltin dilaurate (DBTDL) were purchased from Sigma-Aldrich. The sample materials were prepared by preheating 0.025 mol Poly(tetrahydrofuran) ether glycol (PolyTHF) at 90°C and bubbled with nitrogen for 1 h to remove water and oxygen. Five groups of samples (denoted by A to E) were fabricated with varying molar mass of the backbone molecule to achieve different fracture toughness. Specifically, material A contained 0.025 mol of PolyTHF 250; material B contained 0.015 mol PolyTHF 250 and 0.01 mol PolyTHF 650; material C contained 0.015 mol PolyTHF 250 and 0.01 mol PolyTHF 1000; material D contained 0.015 mol PolyTHF 650 and 0.01 mol PolyTHF 1000; and material E contained 0.015 mol PolyTHF 250 and 0.01 mol PolyTHF 2000. Ethyl acetate (twice weight of PolyTHF) was mixed with the PolyTHF at room temperature under magnetic stirring for 1 h. Then 0.025 mol Isophorone diisocyanate (IPDI) was added into the mixture with magnetic stirring for another 1 h To complete the synthesis, dibutyltin dilaurate (DBTDL, 2% weight of the mixture) was added to the mixture with magnetic stirring for 24 h. During the synthesis process, nitrogen was bubbled in the solution to prevent the reaction between the mixture and the oxygen. After the synthesis process, the obtained solution was poured into a rectangular mold of size 20 mm × 650 mm × 20 mm. The mold was then put into a vacuum chamber for 72 h to evaporate the solvent. After the evaporation process, the elastomer materials can be obtained by separating them from the mold.

The PM10 measurement was carried out by using a self-designed experimental setup (Fig. 2). A stepper motor that can control the rotation speed was purchased from Mophorn. The wheel with a diameter of 20 cm and a thickness of 2 cm was built by 3D printing and was connected to the stepped motor. A clamp with a digital force sensor (LANDTEK FM-204) was purchased from Landtek, and a particle counter (TENMA, 72–10,190) was purchased from TENMA. The sandpapers were purchased from 3M company. All the setups were covered by a box (size: 60 cm × 100 cm × 100 cm) made of acrylic plastics. The polymer samples were glued on the wheel surface with superglue. The sandpaper was cut into square shapes with a size of 15 mm × 15 mm and pressed against the material samples on the wheel by the clamps with the force meter. The particle counter was fixed at 15 cm away from the contact point of the sandpaper and the sample on the wheel. By adjusting the clamps, the contact force between the sample and the sandpaper wheel could be adjusted. During the test, particles with various sizes were emitted by abrasion of the sample material. The particle counter recorded the concentration of particles with diameters of 0.3 μm, 1 μm, 2.5 μm, 5 μm, and 10 μm, respectively. The concentration of PM10 was calculated as the summation of the above groups with particle diameter $\leq$ 10 μm. The speed of stepper motor in the current research was set as 5 rps. Different material samples, different sandpapers (P40, P60, P80, P120, P150, P180, P220) and different contact forces (0.5 N, 1 N, 2 N, 3 N, 4 N, 5 N, 6 N) were tested in current work. As an example, the measured size distributions of the abrasion-emitted particles from five polyurethan elastomer samples are shown in Fig. 3.

To measure the fatigue threshold of the materials, the single-notch method was adopted (Fig. 4). The notched and unnotched samples were prepared in dogbone shapes of width 5 mm, length 10 mm, and thickness 1 mm (Fig. 4ab). The initial crack of length 1 mm on the notched sample was made by the sharp blade. The Dynamic mechanical analyzer (DMA850, TA instrument) was used to conduct cyclic tensile tests on the samples (Fig. 4c). For all the samples, the frequency was set as 5 Hz. In each experiment, cyclic tensile tests were conducted on the unnotched samples with a maximum applied stretch $\lambda_{s_{\max}}$. The curves of nominal stress S_N versus stretch λ_s of the unnotched samples were obtained. The strain energy density under the N-th cycle was calculated as $W(\lambda_{s_{\max}},N) = \int_1^{\lambda_{s_{\max}}} S_N \mathrm{d}\lambda_s$. Then the cyclic tensile tests with same $\lambda_{s_{\max}}$ were conducted on the notched samples. The digital microscope (AM4815ZT, Dino-Lite; resolution, 20 mm/pixel) was used to record the crack length $c(N)$ and crack growth rate $\mathrm{d}c/\mathrm{d}N$on notched samples over the N-th cycle. The applied energy release rate G in the notched sample with the maximum applied stretch of $\lambda_{s_{\max}}$ was calculated as $G(\lambda_{s_{\max}},N) = 2k_s(\lambda_{s_{\max}}) \cdot c(N) \cdot W(\lambda_{s_{\max}},N)$, where $k_s = 3/\sqrt{\lambda_{s_{\max}}}$. For each material, the curve of crack growth rate $\mathrm{d}c/\mathrm{d}N$ versus the applied energy release rate G was acquired by repeating tests with different $\lambda_{s_{\max}}$. The material was considered to reach the fatigue threshold when the applied energy

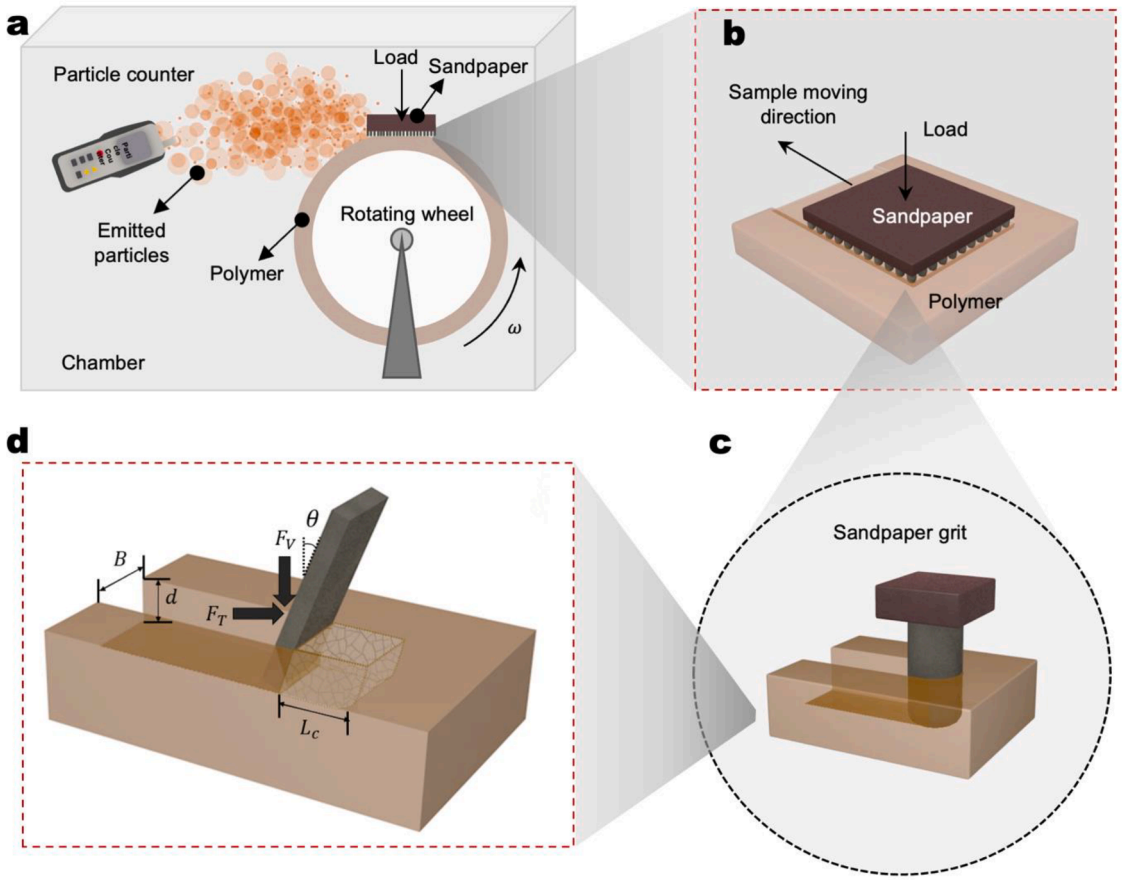

Fig. 2. Experimental setup. (a) The proposed setup for abrasion emission experiments. A motor-controlled rotating wheel with a polymer sample firmly attached to the wheel is housed in a closed chamber. Sandpaper is forced to abrade the moving polymer sample to emit particles that are detected by a particle counter. (b) A zoom-in schematic to illustrate the contact between the sandpaper and the polymer sample. (c) A further zoom-in schematic to illustrate the abrasion fracture induced by a sandpaper grit. (d) A schematic to illustrate the abrasion-induced fracture process.

release rate G began to increase significantly (Fig. 4d). Note that the resolution of $\mathrm{d}c/\mathrm{d}N$ is 0.002 μm/cycle, because the resolution of the digital camera is about 0.02 mm (20 μm/pixel).

Fig. 4e illustrates the fatigue properties of 5 types of polyurethane samples: the crack propagation area rates $\mathrm{d}c/\mathrm{d}N$ for cyclic loads in functions of the corresponding energy release rate G. The dashed lines indicate the fatigue toughness threshold G_c. Qualitatively, with increasing molar mass of PolyTHF within the polyurethane sample, the toughness of the material is decreasing (Fig. 4e), and the

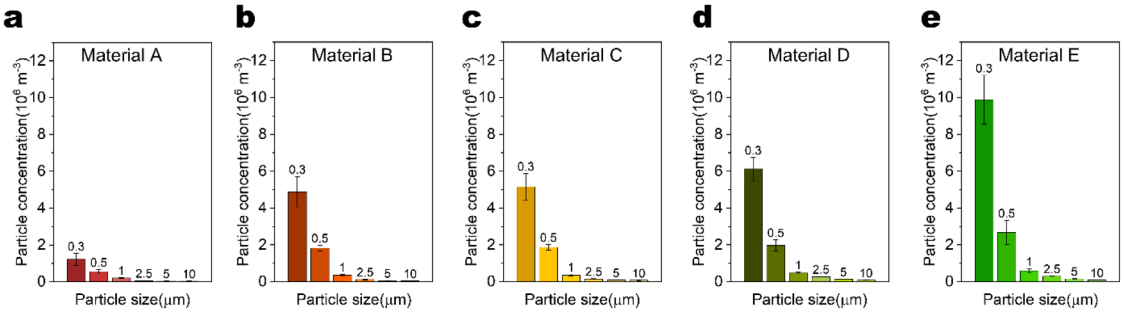

Fig. 3. Size distribution of the abrasion-emitted particles from five polyurethan elastomer samples: (a) material A contained 0.025 mol of PolyTHF 250, (b) material B contained 0.015 mol PolyTHF 250 and 0.01 mol PolyTHF 650, (c) material C contained 0.015 mol PolyTHF 250 and 0.01 mol PolyTHF 1000, (d) material D contained 0.015 mol PolyTHF 650 and 0.01 mol PolyTHF 1000, and (e) material E contained 0.015 mol PolyTHF 250 and 0.01 mol PolyTHF 2000.

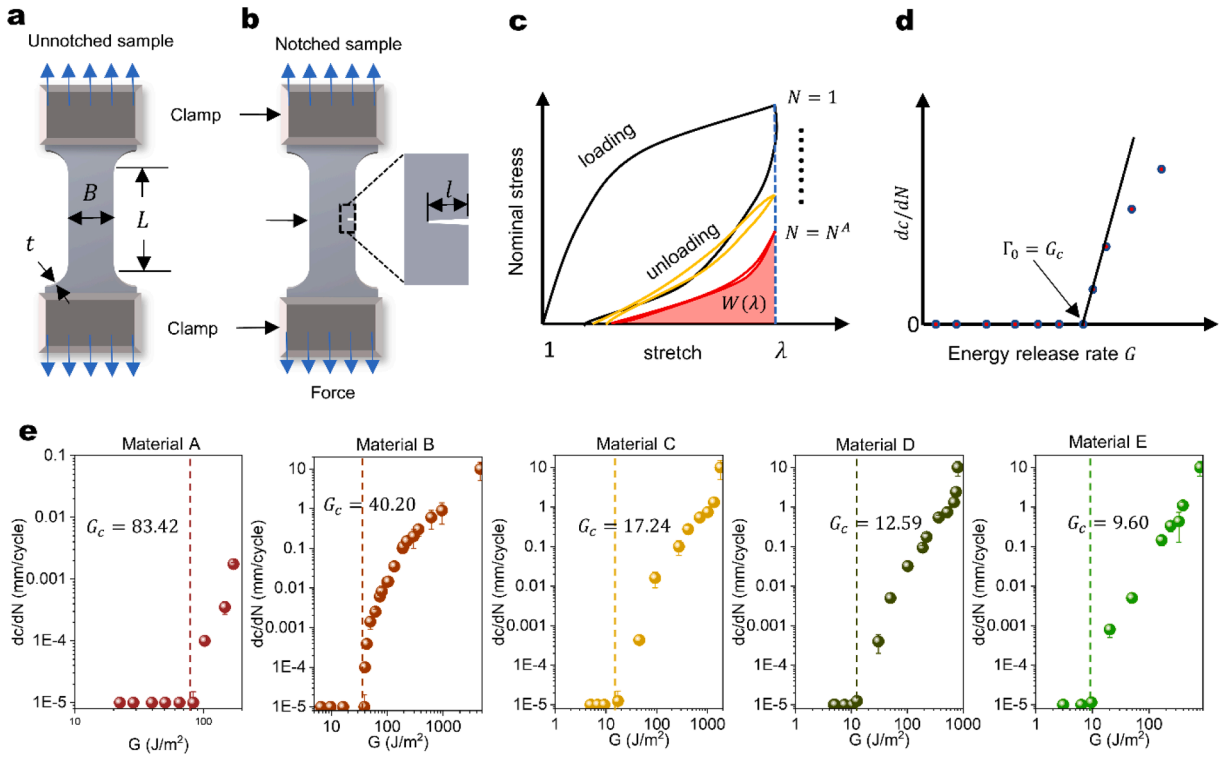

Fig. 4. Measurement of the fatigue property of polymer samples. (ab) Schematics to illustrate the tests on (a) unnotched and (b) notched samples. (c) A schematic to illustrate the stress-stretch behavior of the organic sample under cyclic loadings. (d) A schematic to illustrate a representative relationship between the crack propagation area rate and the energy release rate. The deflection point indicates the fatigue threshold G_c. (d) Fatigue properties of 5 types of polyurethane samples: the crack propagation area rates dc/dN for cyclic loads in functions of the corresponding energy release rate G. The dashed lines indicate the fatigue toughness threshold G_c.

corresponding emitted particle concentration is increasing (Fig. 3). A theoretical framework elaborated in Section 3 will be used to quantitatively explain the emitted particle concentration and the size distribution.

3. Theoretical framework

3.1. Problem statement

In this section, a multiscale theoretical framework is developed to explain the mechanism of particulate matter emission. To capture the essential mechanics, it is claimed that the emission of particulate matter is a direct consequence of fracture propagation in both macroscopic and microscopic scales. During the abrasion process (Fig. 2cd), a groove is formed on the surface of material due to the abrasion and scratch. The generated groove is considered as a fracture surface, on which the strain energy of the elastic body is released. Meanwhile, some micro-cracks are accumulated in accordance with the macroscopic fracture propagation on the groove. the existence and propagation of microcracks are the fundamental reasons for the generation of microparticles during abrasion emission. The microscopically developed cracks considerably reduce the material stiffness, thus affecting the macroscopically propagated fracture as an interplay across both scales. To model the process, the total effective energy release rate G_{total} is ought to account for the macroscopic G and additional G_{add} in the microscopic scale.

In the macroscopic scale, the fracture on the groove is modeled with a boundary value problem within the scope of linear elastic fracture mechanics. The cross section of groove is modeled as a rectangle of width B and depth d, and the fracture length is denoted by L_c (Fig. 2d). The abrasion load consists of a contact force $-F_V$ in the vertical downward direction and frictional force F_T in the horizontal direction. Given the geometry and load, a boundary value problem could be defined in terms of stress, as

$$\begin{cases} \nabla^2\boldsymbol{\sigma} + \dfrac{1}{1+\nu}\nabla\nabla\Theta = \mathbf{0}; \\ \nabla\cdot\boldsymbol{\sigma} = \mathbf{0}; \end{cases} \text{subjected to } \boldsymbol{\sigma}\cdot\mathbf{n} = \mathbf{t},\ \mathbf{x}\in\Omega = \left[-\frac{d}{2},\frac{d}{2}\right]\times\left[-\frac{B}{2},\frac{B}{2}\right]\times[0,L_c], \tag{1}$$

where $\boldsymbol{\sigma}$ is the Cauchy stress tensor, $\Theta = \mathrm{tr}(\boldsymbol{\sigma})$ is the volumetric stress, $\mathbf{n}$ is the outward normal vector of stress boundary, and $\mathbf{t}$ is the traction vector. The first two governing equations in Eq. (1) refer to Beltrami's stress compatibility equation and stress equilibrium

equation, respectively. After the elastic field is fully determined, a path-independent J-integral could be applied to calculate the energy release rate.

3.2. Boundary value problem of macroscopic fracture

3.2.1. Determination of stress components

The schematic illustration in Fig. 2d simplifies the macroscopic model mentioned in the preceding section. A semi-infinite overlay is partially connected to a semi-infinite plane with a macroscopic fracture surface propagating on the interface. It is assumed that the overlay has a uniform cross section of width B and depth d. Additionally, as a quasistatic analysis, the length of the fracture surface is set as a constant L_c. A set of horizontal and vertical boundary tractions F_T and F_V are applied upon the left tip of overlay at $z = 0$. By applying Saint-Venant's principle at the boundary $z = 0$, the following stress boundary conditions and moment boundary conditions are written in the integral form as

$$\begin{cases} F_x(0) = \int \sigma_{zz}|_{z=0} \mathrm{d}A = -F_T; \\ F_y(0) = \int \sigma_{zx}|_{z=0} \mathrm{d}A = F_V; \\ F_z(0) = \int \sigma_{zy}|_{z=0} \mathrm{d}A = 0; \end{cases} \tag{2}$$

$$\begin{cases} M_x(0) = -\int y\sigma_{zz}|_{z=0} \mathrm{d}A = 0; \\ M_y(0) = \int x\sigma_{zz}|_{z=0} \mathrm{d}A = 0; \\ M_z(0) = \int \left(y\sigma_{zx}|_{z=0} - x\sigma_{zy}|_{z=0}\right) \mathrm{d}A = 0. \end{cases} \tag{3}$$

At arbitrary cross section $z = z'$, the moment resulted from the applied force $\mathbf{F} = (-F_V,\ 0,\ F_T)$ on the stress boundary $z = 0$ and the moment resulted from the internal stress $\mathrm{d}\mathbf{t}' = (\sigma_{zx}, \sigma_{zy}, \sigma_{zz})\mathrm{d}A$ on the cross section $z = z'$ must be balanced, which is written as

$$\sum \mathbf{M} = \mathbf{r}_F \times \mathbf{F} + \int_{z=z'} \mathbf{r}_T \times \mathbf{t}' \mathrm{d}A = 0, \tag{4}$$

where $\mathbf{r}_F = (0, 0, -z')$ is the position vector from the plane $z = z'$ to the stress boundary $z = 0$, and $\mathbf{r}_T = (x, y, 0)$ is the position vector from the centroid of section $z = z'$ to arbitrary point on $z = z'$. Similarly, the force balance is written as

$$\sum \mathbf{F} = \mathbf{F} + \int_{z=z'} \mathbf{t}' \mathrm{d}A = 0. \tag{5}$$

From the equilibrium equations in Eqs. (4) and (5), three following equations are obtained explicitly, as

$$\begin{cases} F_T(z) = -\int_{z=z} \sigma_{zz} \mathrm{d}A = F_T; \\ M_x(z) = -\int_{z=z} y\sigma_{zz} \mathrm{d}A = 0; \\ M_y(z) = \int_{z=z} x\sigma_{zz} \mathrm{d}A = 0 = zF_V. \end{cases} \tag{6}$$

Based on the semi-inverse method, we tentatively presume that all in-plane stresses, including σ_{xx}, σ_{yy}, and σ_{xy} vanish, and the remaining σ_{zx}, σ_{zy}, and σ_{zz} are nonzero. Subsequently, the explicit form of normal stress σ_{zz} is hypothesized to take the form of

$$\sigma_{zz} = z(Dx + Qy) + R. \tag{7}$$

By plugging the trial function of σ_{zz} in Eq. (7) into the equilibrium equations in Eq. (6) produces the following three identities.

$$\begin{cases} F_T(z) = -z\int_{z=z} (Dx + Qy)\mathrm{d}A - \int_{z=z} R\mathrm{d}A = -z\left(S_x D + S_y Q\right) - A_c R = F_T; \\ M_x(z) = -z\int_{z=z} \left(Dxy + Qy^2\right)\mathrm{d}A - \int_{z=z} Ry\mathrm{d}A = z\left(I_{xy} D + I_y Q\right) + S_y R = 0; \\ M_y(z) = z\int_{z=z} \left(Dx^2 + Qxy\right)\mathrm{d}A + \int_{z=z} Rx\mathrm{d}A = zF_V, \end{cases} \tag{8}$$

where $I_x = \int y^2 \mathrm{d}A = db^3/12$, $I_y = \int x^2 \mathrm{d}A = bd^3/12$, and $I_{xy} = \int xy \mathrm{d}A$ are components of moment of inertia tensor; $A_c = Bd$ is the cross sectional area. Since the moment of inertia tensor is real symmetric, the diagonalization makes $I_{xy} = 0$ on a principal direction. Because the coordinate is established on the centroid of cross section, both first order moments S_x and S_y are equal to zero. Therefore, the three unknown parameters are solved as

$$D = \frac{F_V}{I_y}, \quad Q = 0, \quad R = -\frac{F_T}{A_c}. \tag{9}$$

Consequently, the normal stress component σ_{zz} is obtained as

$$\sigma_{zz} = \frac{F_V}{I_y} xz - \frac{F_T}{A_c}. \tag{10}$$

By plugging the above Eq. (10) into stress equilibrium equation yields

$$\frac{\partial \sigma_{zx}}{\partial x} + \frac{\partial \sigma_{zy}}{\partial y} + \frac{F_V}{I_y} x = 0. \tag{11}$$

In order to deal with the above identity, a stream function of stress vector is defined as follows.

$$\begin{cases} \sigma_{zx} = \dfrac{\partial F}{\partial y} - \dfrac{F_V}{2I_y} x^2; \\ \sigma_{zy} = -\dfrac{\partial F}{\partial x}. \end{cases} \tag{12}$$

So far, all stress components are expressed in terms of a stream function $F(x,y)$. The following part will be focused on deriving the governing equation and boundary conditions of stream function (Akono and Ulm, 2011).

3.2.2. *Governing equations and boundary conditions of stream function*

The formulation mentioned above is stress-based. The governing equation takes Beltrami-Michell stress compatibility equation, as

$$\nabla^2 \boldsymbol{\sigma} + \frac{1}{1+\nu} \nabla\nabla\Theta = 0, \tag{13}$$

where $\Theta = \mathrm{tr}(\boldsymbol{\sigma}) = \sigma_{zz}$ is a special case for volumetric stress, because $\sigma_{xx} = \sigma_{yy} = 0$ are presumed in the semi-inverse method in last section. By plugging the stress components in Eq. (12) into the stress compatibility equation in Eq. (13) yields

$$\begin{cases} \dfrac{\partial}{\partial y}\left(\nabla^2 F\right) - \dfrac{\nu}{1+\nu} \dfrac{F_V}{I_y} = 0; \\ -\dfrac{\partial}{\partial x}\left(\nabla^2 F\right) = 0. \end{cases} \tag{14}$$

Consequently, the governing equation of stream function is readily obtained by integrating Eq. (14) as

$$\nabla^2 F = \frac{\nu}{1+\nu} \frac{F_V}{I_y} y - 2\mu\alpha, \tag{15}$$

where the additional $-2\mu\alpha$ is an integral constant featuring the torsion effect in Prandtl's stress function. If the shear center coincides the centroid for a highly symmetric cross section, this integral constant vanishes to zero. As a result, the physical meaning is that no warping effect occurs on the cross section during deformation.

With the governing equation obtained in Eq. (15), the following effort will be focused on the determination of boundary conditions. Due to the stress-free condition on the lateral surface and Maxwell's reciprocal theorem, the cross-sectional boundary must be a streamline, which is mathematically written as $(\sigma_{zx}\mathbf{e}_x + \sigma_{zy}\mathbf{e}_y) \times \mathrm{d}\mathbf{s} = \mathbf{0}$. By plugging the stress components of Eq. (12) into the streamline, the streamline differential equation is written explicitly as

$$\begin{vmatrix} & \mathbf{e}_x & & \mathbf{e}_y & \mathbf{e}_z \\ \dfrac{\partial F}{\partial y} - \dfrac{F_V}{2I_y} x^2 & & -\dfrac{\partial F}{\partial x} & & 0 \\ & \mathrm{d}x & & \mathrm{d}y & 0 \end{vmatrix} = \left(\frac{\partial F}{\partial x} \mathrm{d}x + \frac{\partial F}{\partial y} \mathrm{d}y - \frac{F_V}{2I_y} x^2 \mathrm{d}y \right) \mathbf{e}_z = \left(\mathrm{d}F - \frac{F_V}{2I_y} x^2 \mathrm{d}y \right) \mathbf{e}_z = \mathbf{0}. \tag{16}$$

Therefore, the above streamline function indicates that the boundary condition is written as a tangential directional derivative of stream function.

$$\frac{\mathrm{d}F}{\mathrm{d}s}=\frac{F_V}{2I_y}x^2\frac{\mathrm{d}y}{\mathrm{d}s},\quad \text{on } l=\partial\Omega\cap\{(x,y,z):\ \forall z\in(0,L_c)\},\tag{17}$$

where $\partial\Omega$ is the boundary of the region Ω, and l is the boundary of cross section at arbitrary location $0<z<L_c$. The governing equation and boundary condition are demonstrated in Eqs. (15) and (17), and therefore the establishment of boundary value problem has been completed.

3.2.3. Series solution of a rectangular cross-section

In order to solve the above boundary value problem for a rectangular cross section $\boldsymbol{G}$, the governing equation and boundary condition are specified as follows.

$$\nabla^2F=\frac{\nu}{1+\nu}\frac{F_V}{I_y}y\quad \text{on } G,\tag{18}$$

which is subjected to the Neumann boundary conditions as

$$\begin{cases}\dfrac{\partial F}{\partial y}=\dfrac{F_Vd^2}{8I_y}, & x=\pm d/2;\\[2ex] \dfrac{\partial F}{\partial y}=0, & y=\pm b/2.\end{cases}\tag{19}$$

First of all, the non-homogeneous boundary condition at $x=\pm d/2$ is eliminated by introducing an auxiliary function Ψ such that

$$F=\Psi+\frac{F_Vd^2}{8I_y}y.\tag{20}$$

And the boundary conditions in Eq. (19) is formulated with respect to the auxiliary function Ψ, as

$$\begin{cases}\dfrac{\partial\Psi}{\partial y}=0, & x=\pm d\Big/2;\\[2ex] \dfrac{\partial\Psi}{\partial x}=0, & y=\pm b/2.\end{cases}\tag{21}$$

Now it turns out that Ψ is a non-homogeneous Poisson's equation with homogeneous boundary conditions. The homogeneous Neumann boundary conditions indicate that Ψ is a constant value on the boundary, due to the fact that $\mathrm{d}\Psi/\mathrm{d}s=0$. Since the constant value in a potential function does not contribute to the stress, it is reasonable to prescribe $\Psi=0$ on the boundary. Therefore, it is equivalent to applying Dirichlet boundary conditions $\Psi=0$ as opposed to Neumann boundary conditions $\mathrm{d}\Psi/\mathrm{d}s=0$. Next, a particular solution is given as

$$\Psi_p=\frac{\nu F_V}{6(1+\nu)I_y}y\left(y^2-\frac{B^2}{4}\right),\tag{22}$$

which satisfies the boundary condition at $y=\pm b/2$ but does not satisfy the boundary condition at $x=\pm d/2$. Finally, the homogeneous solution of auxiliary function Ψ_h satisfies the following governing equation and boundary condition.

$$\nabla^2\Psi_h=0\quad \text{on } G,\tag{23}$$

which is subjected to the Dirichlet boundary conditions as

$$\begin{cases}\Psi_h=\dfrac{\nu F_V}{6(1+\nu)I_y}y\left(y^2-\dfrac{B^2}{4}\right), & x=\pm d/2;\\ \Psi_h=0, & y=\pm b/2.\end{cases}\tag{24}$$

The general solution could be obtained by separation of variables as $\Psi_h=X(x)Y(y)$, which is written as

$$\Psi_h=\sum_{m=1}^{\infty}A_m\cosh\left(\frac{2m\pi x}{B}\right)\sin\left(\frac{2m\pi y}{B}\right),\tag{25}$$

where the coefficient A_m is determined by the Dirichlet boundary condition at $x=\pm d/2$ and the orthogonality of Fourier series as

$$\begin{aligned} A_m &= -\frac{2}{B}\int_{-B/2}^{B/2}\frac{1}{\cosh(2m\pi d/B)}\frac{\nu F_V}{6(1+\nu)I_y}y\left(y^2-\frac{B^2}{4}\right)\sin\left(\frac{2m\pi y}{B}\right)\mathrm{d}y \\ &= -\frac{(-1)^m B^3}{(m\pi)^3}\frac{1}{\cosh(2m\pi d/B)}\frac{\nu F_V}{4(1+\nu)I_y}. \end{aligned} \tag{26}$$

The general solution of stream function F is superposed as

$$F=\frac{F_V d^2}{8I_y}y+\frac{\nu F_V}{6(1+\nu)I_y}y\left(y^2-\frac{B^2}{4}\right)-\sum_{m=1}^{\infty}\frac{(-1)^m B^3}{(m\pi)^3}\frac{\nu F_V}{4(1+\nu)I_y}\frac{\cosh(2m\pi x/B)}{\cosh(2m\pi d/B)}\sin\left(\frac{2m\pi y}{B}\right). \tag{27}$$

With the aid of Eq. (12), the stress components are determined as

$$\begin{cases} \sigma_{zx}=\dfrac{F_V}{2I_y}\left(\dfrac{d^2}{4}-x^2\right)+\dfrac{\nu F_V}{6(1+\nu)I_y}\left(3y^2-\dfrac{B^2}{4}\right)-\displaystyle\sum_{m=1}^{\infty}\frac{(-1)^m B^2}{(m\pi)^2}\frac{\nu F_V}{2(1+\nu)I_y}\frac{\cosh\left(\dfrac{2m\pi x}{B}\right)}{\cosh\left(\dfrac{2m\pi d}{B}\right)}\cos\left(\frac{2m\pi y}{B}\right); \\ \sigma_{zy}=-\displaystyle\sum_{m=1}^{\infty}\frac{(-1)^m B^2}{(m\pi)^2}\frac{\nu F_V}{2(1+\nu)I_y}\frac{\sinh\left(\dfrac{2m\pi x}{B}\right)}{\cosh\left(\dfrac{2m\pi d}{B}\right)}\sin\left(\frac{2m\pi y}{B}\right); \\ \sigma_{zz}=\dfrac{F_V}{I_y}xz-\dfrac{F_T}{A_c}. \end{cases} \tag{28}$$

It is observed that the stress components σ_{zz} and σ_{zx} are two dominant factors, while the shear stress σ_{zy} in the y direction has minor contribution because the infinite series have absolute convergence. Therefore, the BVP can be approximated as a plane problem by using Filon average in the generalized plane stress problem, as

$$\begin{cases} \sigma_{zx}\approx\overline{\sigma}_{zx}=\dfrac{1}{B}\displaystyle\int_{-B/2}^{B/2}\sigma_{zx}\mathrm{d}y=\frac{6F_V}{Bd^3}\left(\frac{d^2}{4}-x^2\right); \\ \sigma_{zy}\approx\overline{\sigma}_{zy}=\dfrac{1}{B}\displaystyle\int_{-B/2}^{B/2}\sigma_{zy}\mathrm{d}y=0; \\ \sigma_{zz}\approx\overline{\sigma}_{zz}=\dfrac{1}{B}\displaystyle\int_{-B/2}^{B/2}\sigma_{zz}\mathrm{d}y=\frac{12F_V}{Bd^3}xz-\frac{F_T}{Bd}. \end{cases} \tag{29}$$

The above stress components feature the presumption that $\sigma_{yy}=0$, which is equivalent to the plane stress condition. It can be also converted to plane strain condition by introducing $\sigma_{yy}=-\nu\sigma_{zz}$, and thus the strain $\varepsilon_{yy}=0$ will be satisfied. The difference in plane stress and plane strain conditions is presented in the formulation of displacement field, as

$$\begin{cases} \xi_x=\dfrac{1}{E}\left[\kappa\dfrac{\partial\psi}{\partial z}-(1+\nu)\dfrac{\partial\phi}{\partial x}\right]+R_x; \\ \xi_z=\dfrac{1}{E}\left[\kappa\dfrac{\partial\psi}{\partial x}-(1+\nu)\dfrac{\partial\phi}{\partial z}\right]+R_z, \end{cases} \tag{30}$$

where $\kappa=1$ for plane stress condition and $\kappa=1-\nu^2$ for plane strain condition; R_x, R_y are two rigid body displacement functions; and the potential function $\phi(x,z)$ is called Airy's stress function which satisfies

$$\sigma_{xx}=\frac{\partial^2\phi}{\partial z^2};\quad \sigma_{zz}=\frac{\partial^2\phi}{\partial x^2};\quad \sigma_{zx}=-\frac{\partial^2\phi}{\partial x\partial z}. \tag{31}$$

For a differentiable Airy's stress function, there exists a corresponding harmonic function ψ that satisfies

$$\nabla^2\psi=0;\quad \frac{\partial^2\psi}{\partial x\partial z}=\nabla^2\phi. \tag{32}$$

Based on the above requirements, a trial solution of ψ is constructed as

$$\psi(x,z)=\frac{F_V}{bd^3}\left(-\frac{x^4+z^4}{2}+3x^2z^2\right)-\frac{F_T}{bd}xz. \tag{33}$$

So far, the displacement and stress fields have been solved analytically. The next task is to calculate the energy release rate for macro-crack. As in the schematic illustration in Fig. 2, the potential energy change is due to the creation of the new fracture surface $\Omega_s = P_e L_c$, where L_c is the crack length of macro-crack, and $P_e = 2d + B$ is the perimeter edge of the cutter blade.

Then the energy release rate G can be calculated by J integral, which involves the contribution from strain energy density and displacement gradient as

$$G=\frac{1}{P_e}\oint_S\left(un_z-\mathbf{t}\cdot\frac{\partial\boldsymbol{\xi}}{\partial z}\right)\mathrm{d}S, \tag{34}$$

where S is the closed boundary of the volume and $\mathrm{d}S = B\mathrm{d}s$. Then the energy release rate G can be split into two parts as

$$G=J_1+J_2=\frac{B}{P_e}\left(\oint_s un_z\mathrm{d}s\right)+\frac{B}{P_e}\left(\oint_s\mathbf{t}\cdot\frac{\partial\boldsymbol{\xi}}{\partial z}\mathrm{d}s\right), \tag{35}$$

where the strain energy density u is defined via Hooke's law as

$$u=\frac{\kappa}{2E}\sigma_{zz}^2+\frac{1+\nu}{E}\sigma_{zx}^2. \tag{36}$$

The J integral defined in Eq. (35) is calculated as follows:

$$\begin{cases} J_1=-\dfrac{B}{P_e}\displaystyle\int_{-d/2}^{d/2}\left[\frac{\kappa}{2E}\sigma_{zz}^2+\frac{1+\nu}{E}\sigma_{zx}^2\right]\mathrm{d}x=\frac{1}{E\left(1+\dfrac{2d}{B}\right)}\left(-\frac{\kappa F_T^2}{2dB^2}-\frac{6F_V^2(1+\nu)}{5dB^2}\right);\\ J_2=-\dfrac{B}{P_e}\displaystyle\int_{-d/2}^{d/2}\left(\sigma_{zx}\frac{\partial\xi_x}{\partial z}+\sigma_{zz}\frac{\partial\xi_z}{\partial z}\right)\mathrm{d}x=\frac{1}{E\left(1+\dfrac{2d}{B}\right)}\left(\frac{\kappa F_T^2}{dB^2}-\frac{12F_V^2\left(-\dfrac{\kappa}{8}-\dfrac{1+\nu}{2}\right)}{5dB^2}\right);\\ G=J_1+J_2=\dfrac{\kappa}{E\left(B^2d\right)\left(1+\dfrac{2d}{B}\right)}\left(\frac{1}{2}F_T^2+\frac{3}{10}F_V^2\right). \end{cases} \tag{37}$$

To obtain the overall strain energy, the strain energy density in Eq. (36) needs to be integrated as

$$U=\int_{-d/2}^{d/2}\mathrm{d}x\int_0^{L_c}\left(\frac{\kappa}{2E}\sigma_{zz}^2+\frac{1+\nu}{E}\sigma_{zx}^2\right)\mathrm{d}z=\kappa\left(\frac{F_T^2L_c}{2\bar{E}Bd}+\frac{2F_V^2L_c^3}{\bar{E}Bd^3}\right)+(1+\nu)\frac{6F_V^2L_c}{5\bar{E}Bd}. \tag{38}$$

3.3. Effective moduli of a cracked body

The presence of microcracks within a solid continuum can result in a reduction of its effective modulus, consequently altering the energy release rate of the macro-crack under identical loading conditions. Simultaneously, the presence and propagation of micro-cracks in the body may generate additional energy release rates apart from those associated with the macro-crack. In this section, the self-consistent procedure will be described to get the effective moduli of the body with micro-cracks (Budiansky et al., 1976). Results pertaining to both plane stress and plane strain are calculated and discussed.

First let the plane strain condition be considered, and the constitutive law is

$$\varepsilon_x=\frac{1-\nu^2}{E}\left(\sigma_x-\frac{\nu}{1-\nu}\sigma_y\right); \tag{39}$$

$$\varepsilon_y=\frac{1-\nu^2}{E}\left(\sigma_y-\frac{\nu}{1-\nu}\sigma_x\right). \tag{40}$$

To calculate the bulk modulus of a material, we assume an uncracked, homogeneous, isotropic body in a state of uniform hydrostatic pressure p maintained by specified boundary conditions. Then the potential energy of its body can be expressed as $U = -p^2V/2K$, where $K = E/2(1+\nu)(1-2\nu)$ is the bulk modulus of the material and V is the total volume. After the introduction of random oriented cracks, the effective bulk modulus $\bar{K}$ of the cracked body and the potential energy change has the relation as (Garbin and Knopoff, 1973)

$$-\frac{p^2V}{2\overline{K}} = -\frac{p^2V}{2K} + \Delta U. \tag{41}$$

By dimensional analysis, this energy loss must take the form of

$$\Delta U = -\frac{p^2a^3}{\overline{E}} f(\bar{\nu}), \tag{42}$$

where a is the characteristic linear crack dimension, $\bar{\nu}$ is the effective Poisson's ratio, $\overline{E}$ is the effective Young's modulus of the cracked body, and f is a non-dimensional shape factor depending on the crack shape and $\bar{\nu}$. We assume that a single isolated crack has the same effect on the energy change in an infinite medium as in a cracked body and ignore the interaction between cracks. The energy change after the introduction of the micro-cracks is

$$\Delta U = -\frac{p^2}{\overline{E}} n\langle a^3 f(\bar{\nu})\rangle \tag{43}$$

where n is the number of micro cracks per unit volume, and the angle bracket denotes an average operator with respect to the crack length and orientation (Sun and Ju, 2004).

Because the cracked body is still isotropic, and in plane stain condition, $\overline{E}$ and $\overline{K}$ have the relation as

$$\frac{\overline{E}}{\overline{K}} = 2(1+\bar{\nu})(1-2\bar{\nu}) \tag{44}$$

By substituting Eqs. (43), (44) into Eq. (41), the effective bulk modulus can be yielded as

$$\frac{\overline{K}}{K} = 1 - \frac{n\langle a^3 f(\bar{\nu})\rangle}{(1+\bar{\nu})(1-2\bar{\nu})}. \tag{45}$$

By assuming that the no correlation exists between crack size and shape, Eq. (45) can be reduced to (Budiansky et al., 1976) (Hoenig, 1979)

$$\frac{\overline{K}}{K} = 1 - \frac{n\langle a^3\rangle\langle f(\bar{\nu})\rangle}{(1+\bar{\nu})(1-2\bar{\nu})}. \tag{46}$$

The process of calculation of effective Young's modulus $\overline{E}$ is quite similar by introduction of a uniaxial tension t_s. The $\overline{E}$ can be expressed using Eqs. (39) and (40) in plain strain as

$$-\frac{(1-\bar{\nu}^2){t_s}^2V}{2\overline{E}} = -\frac{(1-\nu^2){t_s}^2V}{2E} + \Delta U. \tag{47}$$

Because the potential energy can be affected by the resolved stresses σ and τ which are normal and tangential to the plane of the crack, so the energy change should have the form of (Laws and Brockenbrough, 1987)

$$\Delta U = -\frac{a^3}{\overline{E}}\left[\sigma^2 f(\bar{\nu}) + \tau^2 g(\bar{\nu})\right], \tag{48}$$

where $f(\bar{\nu})$ and $g(\bar{\nu})$ are non-dimensional shape factors that only depend on $\bar{\nu}$. According to the coordinate transformation, the resolved stress can be expressed as

$$\sigma = t_s\cos^2\alpha; \tag{49}$$

$$\tau = t_s\sin\alpha\cos\alpha. \tag{50}$$

Substituting Eqs. (49) and (50) into Eq. (48), the energy change can be expressed as

$$\Delta U = -\frac{a^3}{\overline{E}}\left[t_s^2\cos^4\alpha f(\bar{\nu}) + t_s^2\sin^2\alpha\cos^2\alpha g(\bar{\nu})\right]. \tag{51}$$

The effective $\overline{E}$ can be derived by substituting Eq. (51) into Eq. (47), written as

$$\frac{\overline{E}}{E} = \frac{1-\bar{\nu}^2}{1-\nu^2}\left[1 - \frac{2n\langle a^3\rangle\left\langle\cos^4\alpha f(\bar{\nu}) + \sin^2\alpha\cos^2\alpha g(\bar{\nu})\right\rangle}{1-\bar{\nu}^2}\right]. \tag{52}$$

Because the micro-cracks are randomly oriented with uniform distribution, the average of the following trigonometric functions can be defined and calculated as

$$\langle\cos^4\alpha\rangle = \frac{\oint\cos^4\alpha\,\mathrm{d}s}{\oint 1\,\mathrm{d}s} = \frac{3}{8}; \tag{53}$$

$$\langle \sin^2\alpha\cos^2\alpha \rangle = \frac{\oint \sin^2\alpha\cos^2\alpha \mathrm{d}s}{\oint 1\mathrm{d}s} = \frac{1}{8}. \tag{54}$$

With the aid of angle average on a unit circle that is explicitly given in Eqs. (53) and (54), the expression of the effective $\overline{E}$ can be to

$$\frac{\overline{E}}{E} = \frac{1-\overline{\nu}^2}{1-\nu^2}\left[1 - \frac{n\langle a^3\rangle}{4(1-\overline{\nu}^2)}\left(3\langle f(\overline{\nu})\rangle + \langle g(\overline{\nu})\rangle\right)\right]. \tag{55}$$

Consider the introduction of single isolated crack with length of $2a$ in an infinite medium, for two dimensional cracks, the stress intensity factors K_I and K_{II} (Gdoutos, 2020) can be written as

$$\begin{cases} K_I = \sigma\sqrt{\pi a}; \\ K_{II} = \tau\sqrt{\pi a}. \end{cases} \tag{56}$$

The energy release rate has the relations with K_I K_{II} as

$$G = \kappa\left(\frac{K_I^2}{E} + \frac{K_{II}^2}{E}\right), \tag{57}$$

where $\kappa = 1$ for plane stress and $\kappa = 1-\nu^2$ for plane strain. By substituting Eq. (56) into Eq. (57), the G can be expressed as

$$G = \left(1-\overline{\nu}^2\right)\left(\frac{\sigma^2+\tau^2}{E}\right)\pi a. \tag{58}$$

The relation between G and the energy change ΔU is defined as

$$G = \frac{1}{B}\frac{\mathrm{d}(\Delta U)}{\mathrm{d}(2a)}, \tag{59}$$

where B is the thickness of the material. Then the energy change can be calculated by integrating Eq. (58) as

$$\Delta U = \frac{(1-\nu^2)}{E}\left(\sigma^2+\tau^2\right)a^2 B. \tag{60}$$

For an isotropic body in a state of hydrostatic stress p, it is readily obtained that $\sigma = p$ and $\tau = 0$. Comparing Eq. (60) with Eq. (42), we can obtain $f(\overline{\nu})$ as

$$f(\overline{\nu}) = \left(1-\overline{\nu}^2\right)\pi\left(\frac{B}{a}\right). \tag{61}$$

For an isotropic body in a state of a uniaxial tension s, comparing Eq. (60) with the Eq. (48), $g(\overline{\nu})$ can be obtained as

$$g(\overline{\nu}) = \left(1-\overline{\nu}^2\right)\pi\left(\frac{B}{a}\right). \tag{62}$$

Substituting Eqs. (61) and (62) into Eq. (46), the effective bulk modulus $\overline{K}$ can be calculated as

$$\frac{\overline{K}}{K} = 1 - \frac{n\langle a^3 f(\overline{\nu})\rangle}{(1+\overline{\nu})(1-2\overline{\nu})} = 1 - \frac{n\pi B\langle a^2\rangle(1-\overline{\nu})}{1-2\overline{\nu}}. \tag{63}$$

The same procedure can be applied to obtain the effective Young's modulus $\overline{E}$ by substituting Eqs. (61), (62) into Eq. (55) as

$$\frac{\overline{E}}{E} = \frac{1-\overline{\nu}^2}{1-\nu^2}\left(1 - n\pi B\langle a^2\rangle\right). \tag{64}$$

Because the cracked body is still isotropic, $\overline{\nu}$ can be obtained by combining Eqs. (63), (64), and (44) as

$$\overline{\nu} = 1 - \frac{1-\nu}{1-\nu\epsilon}. \tag{65}$$

where ϵ is the crack density which is defined as $\epsilon = n\pi B\langle a^2\rangle$.

The above is the derivation of the effective modulus of the cracked body under plane strain condition, and the results can be summarized as follows:

$$\begin{cases} \dfrac{\overline{K}}{K} = 1 - \dfrac{1-\overline{\nu}}{1-2\overline{\nu}}\epsilon; \\ \dfrac{\overline{E}}{E} = \dfrac{1-\overline{\nu}^2}{1-\nu^2}(1-\epsilon); \\ \overline{\nu} = 1 - \dfrac{1-\nu}{1-\nu\epsilon}. \end{cases} \tag{66}$$

The similar derivation procedure can be applied to plane stress conditions, and thus critical results are provided without detailed derivation. In plane stress, the constitutive law is

$$\begin{cases} \boldsymbol{\varepsilon}_{xx} = \dfrac{1}{\boldsymbol{E}}\left(\boldsymbol{\sigma}_x - \boldsymbol{\nu}\boldsymbol{\sigma}_y\right); \\ \boldsymbol{\varepsilon}_{yy} = \dfrac{1}{\boldsymbol{E}}\left(\boldsymbol{\sigma}_y - \boldsymbol{\nu}\boldsymbol{\sigma}_x\right); \\ \boldsymbol{\varepsilon}_{xy} = \dfrac{1+\boldsymbol{\nu}}{\boldsymbol{E}}\boldsymbol{\tau}_{xy}. \end{cases} \tag{67}$$

The relations between $\overline{E}$ and $\overline{K}$ under the plane stress condition is

$$\frac{\overline{E}}{\overline{K}} = 2(1-\overline{\nu}). \tag{68}$$

By introducing randomly oriented cracks, the effective bulk modulus $\overline{K}$ of the cracked body and the potential energy change has the relations same with Eq. (41). The effective bulk modulus should have the following form as

$$\frac{\overline{K}}{K} = 1 - \frac{n\langle a^3\rangle\langle f(\overline{\nu})\rangle}{1-\overline{\nu}}. \tag{69}$$

The effective Young's modulus is expressed as

$$\frac{\overline{E}}{E} = 1 - 2n\,\langle a^3\rangle\left[\frac{3}{8}\,\langle f(\overline{\nu})\rangle + \frac{1}{8}\,\langle g(\overline{\nu})\rangle\right]. \tag{70}$$

The non-dimensional factors $f(\overline{\nu})$ and $g(\overline{\nu})$ can be calculated as

$$\begin{cases} f(\overline{\nu}) = \pi\left(\dfrac{B}{a}\right); \\ g(\overline{\nu}) = \pi\left(\dfrac{B}{a}\right). \end{cases} \tag{71}$$

By substituting Eq. (71) into Eqs. (69) and (70), the effective modulus of cracked body under the plane stress condition can be calculated as

$$\frac{\overline{K}}{K} = 1 - \frac{\epsilon}{1-\overline{\nu}}; \tag{72}$$

$$\frac{\overline{E}}{E} = 1 - \epsilon. \tag{73}$$

Combining Eqs. (68), (72) and (73), $\overline{\nu}$ can be calculated. And the results for plane stress can be summarized as

$$\begin{cases} \dfrac{\overline{K}}{K} = 1 - \dfrac{\epsilon}{1-\overline{\nu}}; \\ \dfrac{\overline{E}}{E} = 1 - \epsilon; \\ \overline{\nu} = \nu(1-\epsilon). \end{cases} \tag{74}$$

3.4. Additional energy release rate model

The previous abrasion model only accounts for the energy release rate associated with the macro-crack. Although this model can roughly explain the material detachment process, it fails to adequately elucidate the physical mechanisms underpinning PM10 generation and release. Building upon the abrasion model elaborated in Section 3.2, the abraded region is treated as a cracked body with micro-cracks. The presence and propagation of micro-cracks within the body can contribute additional energy release rates beyond that due to the macro-crack. Due to the random nature of the micro-cracks within the abrasion body, the derivation for the additional

energy release rate due to the micro-cracks is technically challenging. In order to roughly estimate the additional energy release rate, here we propose a method based on the definition of the energy release rate.

From previous sections, the strain energy of uncracked body under the condition of plane strain has been calculated in Eq. (38). By substituting E with $\overline{E}$ and ν with $\overline{\nu}$, the strain energy of the cracked body in plane strain can be expressed as

$$U = \left(1-\overline{\nu}^2\right)\left(\frac{F_T^2 L_c}{2\overline{E}Bd} + \frac{2F_V^2 L_c^3}{\overline{E}Bd^3}\right) + \left(1+\overline{\nu}\right)\frac{6F_V^2 L_c}{5\overline{E}Bd}. \tag{75}$$

We define the additional energy release rate as how much energy released when the micro-cracks propagate by a unit area. Since the crack process is force-controlled here, we can estimate the additional energy release rate as

$$G_{add} = \frac{\partial U}{\partial B\langle a\rangle}. \tag{76}$$

Note that there should be a minus sign when the crack process is a displacement-controlled.

With the aid of chain rule, the G_{add} can be expressed as

$$\frac{\partial U}{\partial \langle a\rangle} = \frac{\partial U}{\partial \epsilon}\frac{\partial \epsilon}{\partial \langle a\rangle}. \tag{77}$$

By substituting Eq. (66) into Eq. (75) and eliminating the $\overline{E}$ and $\overline{\nu}$ in Eq. (75) produces

$$\frac{\partial U}{\partial \epsilon} = \left(1-\nu^2\right)\frac{1}{E}\left[\frac{F_T^2 L_c}{2Bd} + \frac{2F_V^2 L_c^3}{Bd^3} + \frac{6F_V^2 L_c}{5Bd}\right]\frac{1}{(1-\epsilon)^2}. \tag{78}$$

The additional energy release rate G_{add} for plain strain can be calculated by substituting $\partial\epsilon/\partial\langle a\rangle = 2n\pi B\langle a\rangle$ into the Eq. (76) as

$$G_{add} = \frac{\partial U}{\partial B\langle a\rangle} = \left(1-\nu^2\right)\frac{1}{E}\left[\frac{F_T^2 L_c}{2Bd} + \frac{2F_V^2 L_c^3}{Bd^3} + \frac{6F_V^2 L_c}{5Bd}\right]\frac{2n\pi\langle a\rangle}{(1-\epsilon)^2}. \tag{79}$$

The same derivation can be applied to plain stress conditions. The strain energy of the cracked body in plain stress can be expressed as

$$U = \frac{F_T^2 L_c}{2\overline{E}Bd} + \frac{2F_V^2 L_c^3}{\overline{E}Bd^3} + \frac{6(1+\overline{\nu})F_V^2 L_c}{5\overline{E}Bd}. \tag{80}$$

By substituting Eq. (66) into Eq. (75) and eliminating the $\overline{E}$ and $\overline{\nu}$ in Eq. (75), G_{add} for plain stress condition can be calculated as

$$G_{add} = \frac{\partial U}{\partial B\langle a\rangle} = \frac{1}{E}\left[\frac{F_T^2 L_c}{2Bd} + \frac{2F_V^2 L_c^3}{Bd^3} + \frac{6F_V^2 L_c}{5Bd}\right]\frac{2n\pi\langle a\rangle}{(1-\epsilon)^2}. \tag{81}$$

Notice that the results of G_{add} in plain strain differ from results in plain stress by a coefficient $(1-\nu^2)$, and therefore we can merge the results into a general form as

$$G_{add} = \frac{\partial U}{\partial B\langle a\rangle} = \frac{\kappa}{E}\left[\frac{F_T^2 L_c}{2Bd} + \frac{2F_V^2 L_c^3}{Bd^3} + \frac{6F_V^2 L_c}{5Bd}\right]\frac{2n\pi\langle a\rangle}{(1-\epsilon)^2}. \tag{82}$$

Where $\kappa = 1$ for the plane strain condition and $\kappa = (1-\nu^2)$ for plane stress condition.

Then consider that the characteristic crack length of i^{th} micro crack can be expressed as $a_i = \langle a\rangle + \Delta a_i$, where Δa_i is the i^{th} difference to the average micro-crack length. By substituting $\langle a\Delta a_i\rangle = 0$ (Grimmett and Stirzaker, 2020), we can get

$$\left\langle a^2\right\rangle = \left\langle \langle a\rangle^2 + 2a\Delta a + \Delta a^2\right\rangle = \langle a\rangle^2 + \left\langle \Delta a^2\right\rangle, \tag{83}$$

where $\langle a\rangle$ is the average of the micro crack lengths and $\langle \Delta a^2\rangle$ is the variance of the micro crack lengths.

Then the expression of G_{add} can be reduced to

$$G_{add} = \frac{\partial U}{\partial B\langle a\rangle} = \frac{\kappa}{E}\left[\frac{F_T^2 L_c}{2Bd} + \frac{2F_V^2 L_c^3}{Bd^3} + \frac{6F_V^2 L_c}{5Bd}\right]\frac{2n\pi\langle a\rangle}{(1-n\pi B(\langle a\rangle^2 + \langle \Delta a^2\rangle))^2}. \tag{84}$$

The total energy release rate can be calculated by superposing energy release rate associated with the macro-crack and the additional energy release rate associated with micro-cracks, which is written as

$$G_{total} = \frac{\kappa}{\overline{E}\left(B^2 d\right)\left(1+\frac{2d}{B}\right)}\left(\frac{1}{2}F_T^2 + \frac{3}{10}F_V^2\right) + \frac{\kappa}{E}\left[\frac{F_T^2 L_c}{2Bd} + \frac{2F_V^2 L_c^3}{Bd^3} + \frac{6F_V^2 L_c}{5Bd}\right]\frac{2n\pi\langle a\rangle}{(1-n\pi B(\langle a\rangle^2 + \langle \Delta a^2\rangle))^2}, \tag{85}$$

where $\overline{E}/E = 1-\epsilon$ for the plane stress condition and $\overline{E}/E = \frac{1-\overline{\nu}^2}{1-\nu^2}(1-\epsilon)$ for the plane strain condition. If we assume that the micro-crack length agrees with the particle size of the PM10 released, the $\langle a\rangle$ can be regarded as the average particle size of PM10 and $\langle \Delta a^2\rangle$ can be

regards as the variance of the PM10, which is the square of the standard deviation. Thus the Eq. (85) establish a relation between the fracture mechanics and the distribution characteristic of PM10.

3.5. Overall problem-solving process

The developed model elucidates the process of PM10 emission, establishing a quantitative relationship between fracture mechanics and PM10 emission. In this section, with the knowledge of loading conditions, we employ the established mechanics model to calculate the particle size distribution of PM10. The overall problem-solving process is shown in Fig. 5.

The first step is to assume that the particle size distribution of the PM10 released into air obeys Weibull distribution with parameters λ and k, where λ is the scale parameter and k is the shape parameter (Austin et al., 1984; Rosin, 1933). We adopt Weibull distribution because the shape of the particle size distributions shown in Fig. 2 resembles that of Weibull distribution. The probability density function of the Weibull distribution is given as

$$f(x,\lambda,k)=\begin{cases}\dfrac{k}{\lambda}\left(\dfrac{x}{\lambda}\right)^{k-1}e^{-\left(\frac{x}{\lambda}\right)^{k}}, & x\geq 0;\\ 0, & x<0.\end{cases} \tag{86}$$

Using the Weibull distribution to describe the size distribution, the average and the variance of the particle size of PM10 can be calculated as (Austin et al., 1984; Rosin, 1933)

$$\langle a\rangle=\lambda\Gamma\left(1+\frac{1}{k}\right); \tag{87}$$

$$\left\langle \Delta a^{2}\right\rangle=\lambda^{2}\left[\Gamma\left(1+\frac{1}{k}\right)-\Gamma\left(1+\frac{1}{k}\right)^{2}\right], \tag{88}$$

where Γ is the Gamma function.

The next step is to link the distribution parameters λ and k to the fracture process. It is reasonable to assume that the total particle number per volume of the air N_{total} is linearly proportional to the particle number per volume of the solid material $N_{particle}$. Thus, N_{total}can be expressed as

$$N_{total}=\beta N_{particle}, \tag{89}$$

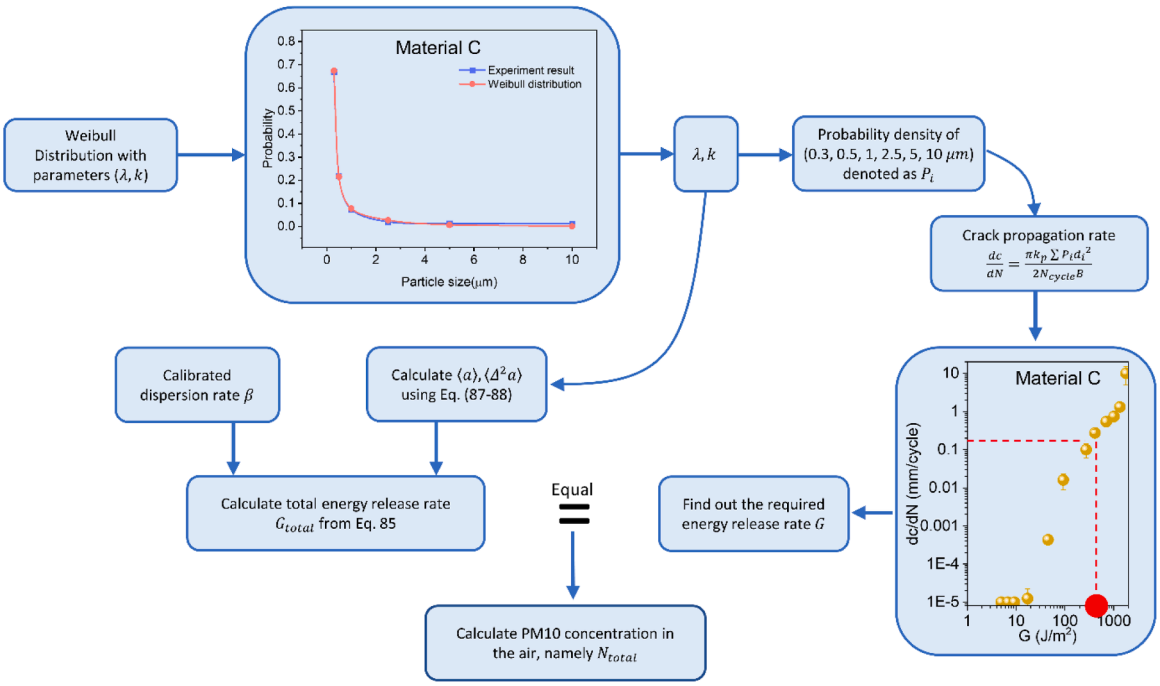

Fig. 5. The overall structure of the problem-solving framework.

where β is the dispersion rate from solid material to air. Within the solid material, we assume that the particle number per volume $N_{particle}$ linearly scales with the crack number per unit volume n written as

$$N_{particle} = k_p n. \tag{90}$$

where k_p is a constant to indicate the topological relationship between the crack and the particle. To simplify the overall framework, we here only assume a 2D rectangular topology model to reveal the relationship between the crack particle density and the crack density (Fig. 6). As illustrated in Fig. 6, we can simply obtain $k_p = 2$.

From Eqs. (89) to (90), N_{total}can be written as

$$N_{total} = k_p \beta n. \tag{91}$$

During the fatigue fracture process, $\frac{dc}{dN}N_{cycle}$ represents the total fracture length within the material. Since there will be two fracture surfaces generated when a single microcrack propagates, the total fracture surface per volume of micro cracks within the solid material $S_{microcracks}$ can be expressed as,

$$S_{microcracks} = 2\frac{dc}{dN}N_{cycle}nB, \tag{92}$$

where N_{cycle} is the cycle number, n is the micro-crack number per unit volume of the solid material, and B is the width of the solid material.

At the same time, the total particle surface area per volume of the air can be expressed as

$$S_{particle} = \pi N_{total} \sum P_i d_i^2, \tag{93}$$

where P_i is the probability measure of particle with a diameter of $d = d_i$ in the air.

When the solid material is worn out and turns into particles floating in the air, the volume occupied by the particles in the solid material is different from that in the air as there is a dispersion process. The total fracture surface of microcracks per volume within the solid material $S_{microcracks}$ can be converted into the total surface of particles per volume of the air $S_{particle}$ by using the dispersion rate β, written as $S_{particle} = \beta S_{microcracks}$, which can be rewritten as

$$\pi N_{total} \sum P_i d_i^2 = 2\beta \frac{dc}{dN} N_{cycle} nB. \tag{94}$$

Substituting Eq. (91) into Eq. (94), the dc/dN can be calculated as

$$\frac{dc}{dN} = \frac{\pi k_p \sum P_i d_i^2}{2N_{cycle}B}. \tag{95}$$

In order to obtain dc/dN, the summation $\sum P_i d_i^2$ has to be obtained first. Air pollutants are usually classified into PM0.3, PM0.5, PM1, PM2.5, PM5, and PM10, referring to the air pollutants with the diameter of 0.3μm, 0.5μm, 1μm, 2.5μm, 5μm, and 10μm respectively. The cumulative distribution function of the Weibull distribution can be written as

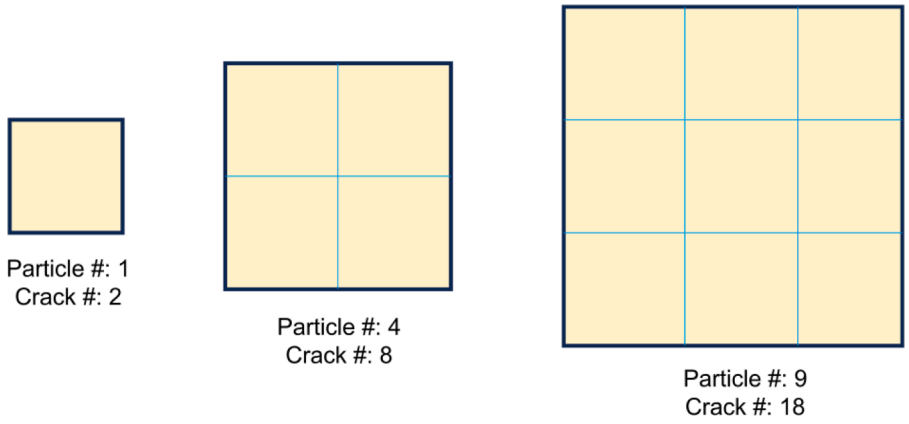

Fig. 6. A 2D rectangular topology model to illustrate the relationship between the particle number and the crack number. The lateral denotes the crack. The laterals on the boundary only share half weight.

$$F(x) = \begin{cases} 1 - e^{-\left(\frac{x}{\lambda}\right)^k}, & x \geq 0; \\ 0, & x < 0. \end{cases} \tag{96}$$

Because the Weibull distribution is a continuous distribution, we need to discretize it to obtain a discrete distribution under each particle size P_i. The discrete principle are as follows. Suppose we need to get the discrete distribution at points $d = d_i$ written as $P_{d_i} = P(d = d_i)$, the probability mass function of discrete diameter d_i can be defined as

$$P_{d_i} = F(d_i - 1/2(d_i - d_{i-1})) - F(d_i + 1/2(d_{i+1} - d_i)). \tag{97}$$

In our case, for example, the probability of 1 μm is defined as $F(1.75) - F(0.75)$, and the probability of 2.5 μm is defined as $F(3.75) - F(1.75)$. From the above definition, once the parameter λ and k are determined, the $P_{0.3}, P_{0.5}, P_1, P_{2.5}, P_{2.5}, P_5$, and P_{10} can be calculated. Thus, by substituting the P_i into Eq. (95), $\mathrm{d}c/\mathrm{d}N$ can be obtained.

Then the next step is to obtain the total energy release rate G_{total} from $\mathrm{d}c/\mathrm{d}N$. Based on the fatigue property of the polymers as shown in Fig. 4e, the relationship between the fatigue crack growth rate $\mathrm{d}c/\mathrm{d}N$ and the energy release rate G_{total} obeys a power law after the transition regime, which is written as

$$\lg\left(\frac{\mathrm{d}c}{\mathrm{d}N}\right) = K \lg G_{total} - b, \tag{98}$$

where K and b are material parameters that are determined by experiments. Based on Eq. (98), the predicted energy release rate G_{total} can be obtained.

Then we can try to obtain the predicted total particle number per volume N_{total} from predicted energy release rate G_{total}. From Eq. (85), G_{total} is a function of following variables, which can be written as

$$G_{total} = f\left(F_T,\ F_V,\ B,\ d,\ L_c,\ n,\ \langle a \rangle,\ \left\langle \Delta a^2 \right\rangle\right), \tag{99}$$

where F_T, F_V, B, d, L_c can be experimentally determined. Upon determining the value of λ, k, the average $\langle a \rangle$ and variance of the $\langle \Delta a^2 \rangle$ can be ascertained. According to Eq. (99), the micro-crack number per volume of the solid material n can be obtained. Based on the relation of n and N_{total} shown in Eq. (91), if the dispersion rate is properly selected, the concentration of particles in the air N_{total} can be obtained. Therefore, the distribution and the total number of the particles can be calculated (Fig. 5).

4. Results

4.1. Theoretical results for micromechanical model of cracked body

This section presents the theoretical results for a micromechanical model of a cracked body, which is elaborated in Section 3.3. The presence of microcracks in the body leads to a change in both the effective Young's modulus and Poisson's ratio. The theoretical results for both plane stress and plane strain conditions are provided for a cracked body with an original Poisson's ratio of 0.1, 0.2, 0.3, 0.4, and 0.5.

The ratio between the effective Young's modulus and the original Young's modulus, denoted as $\overline{E}/E$, decreases with increasing crack densities for both plane stress and plane strain conditions (Fig. 7a). According to the equation Eq. (73), under the plane stress condition, $\overline{E}/E$ is linearly proportional to the crack density and is not associated with the Poisson's ratio. Thus, the relation between $\overline{E}/E$ and ϵ is shown as a straight line in Fig. 7a. However, under plane strain conditions, $\overline{E}/E$ are concave curves and the rate of decrease in effective Young's modulus changes with the original Poisson's ratio. Similar trends apply to the effective Poisson's ratio results. In the plane stress condition (Fig. 7b), the ratio between the effective Poisson's ratio and the original Poisson's ratio, denoted as $\overline{\nu}/\nu$,

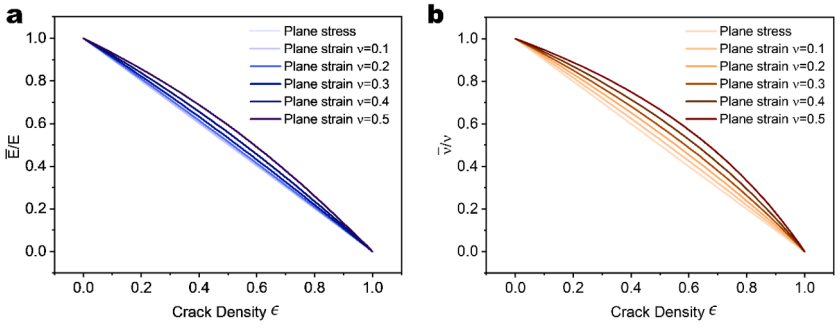

Fig. 7. Mechanical properties of cracked body. (A) Effective young's modulus of cracked body in a function of the crack density. (B) Effective Poisson's ratio of the cracked body in a function of the crack density.

Table 1
Employed parameters for the calculation for Figs. 8, 9. The estimation basis is given for each parameter. Fracture length of macro-crack L_c, the width of the fracture groove of the macro-crack B, and the depth of the fracture groove of the macro-crack d are estimated to be on the same scale of the grit size which is considered as the length scale associated with the surface roughness. For simplicity, we here estimate them to be equal to the mean grit size (~100 μm). Note that the mean grit sizes are different for different types of sandpaper used in experiments for Fig. 13, and we thus estimate L_c, B, and d as the respective grit sizes for different sandpaper in Fig. 13. The vertical traction on each grit F_V is estimated by using $F_V = F_C / N_S$, where F_C is the vertical contact force applied on the sample which can be measured by a force gage, and N_S is the number of sandpaper grits sustaining the vertical force. Horizontal traction on each grit F_T is estimated by using $F_T = \kappa F_V$, where κ is the kinetic friction coefficient between the material and the sandpaper which is measured by experiments. The measured friction coefficients for various materials and sandpaper are shown in Table 2.

Parameter	Physical meaning	Value	Basis
$\langle a \rangle$ (m)	Average length of micro-cracks	5.235×10^{-7}	Experiment
$\langle \Delta a^2 \rangle$ (m^2)	Average variance of the micro-cracks	8.497×10^{-13}	Experiment
E (MPa)	Young's modulus of material	5.80308	Experiment
F_T (N)	Horizontal traction on each grit	0.05	Calculation
F_V (N)	Vertical traction on each grit	0.053	Calculation
L_c (m)	Fracture length of macro-crack	10^{-4}	Estimated from grit size
B (m)	The width of the fracture groove of the macro-crack	10^{-4}	Estimated from grit size
d (m)	The depth of the fracture groove of the macro-crack	10^{-4}	Estimated from grit size
N_{total} (m^{-3})	Total particle number per unit volume in the air	7.297×10^6	Experiment
β	Dispersion rate from solid material to air	7.92447×10^{-9}	Calibrated

Table 2
The mean diameter and standard deviation of the grit diameter of various types of sandpaper, and the measured kinetic friction coefficients between these sandpaper and various polyurethane samples.

Sandpaper type (3M company)	Mean diameter (μm)	Standard deviation (μm)	Kinetic friction coefficient (Material A)	Kinetic friction coefficient (Material B)	Kinetic friction coefficient (Material C)	Kinetic friction coefficient (Material D)	Kinetic friction coefficient (Material E)
120	120.22	10.19	0.9622	0.9712	0.9832	0.9934	1.0231
150	100.12	8.42	0.9254	0.9323	0.9473	0.9582	0.9622
180	79.92	7.41	0.8982	0.9083	0.9162	0.9283	0.9321
220	61.92	5.32	0.8610	0.8793	0.8723	0.8910	0.8982

scales linearly with the crack density and is independent of the original Poisson's ratio. Conversely, in the plane strain condition, the rate of decrease in effective Poisson's ratio changes with the original Poisson's ratio.

4.2. *Effects of variables on energy release rates*

Next, we study the effect of variables including Young's modulus E, scratch depth d, vertical force F_V, and horizontal force F_T on the total energy release rate G_{total} and additional energy release rate G_{add}. The parameters we employed is shown in Tables 1, 2. We first study the effect of Young's modulus on the total and additional energy release rates (Fig. 8a). As Young's modulus increases, both the total energy release rate and the additional energy release rate decrease, while the ratio between the additional energy release rate and the total energy release rate G_{add}/G_{total} remains as ~22 % regardless of the change of Young's modulus. The decreasing trend is because that under the same abrasion loading, namely vertical force F_V, and horizontal force F_T, the abrasion on the stiffer material is accordingly more difficult.

Then, we examine the effect of the scratch depth d on the energy release rates (Fig. 8b). We find that the total energy release rate and the additional energy release rate follow similar patterns as the scratch depth d increases, initially exhibiting a sharp decline, followed by a deceleration in the rate of decrease. The decreasing trend reveals that the abrasion on the material becomes more difficult as the abrasion depth increases.

In Fig. 8cd, we examine the effects of the horizontal and vertical forces on the energy release rates. It is found that both the total energy release rate and the additional energy release rate increase as either horizontal or vertical force increases. However, there exists a disparity in their response to the two types of forces. Specifically, as the vertical force rises, there is a significant augmentation in the additional energy release rate (Fig. 8c), whereas an increase in the horizontal force does not result in a noteworthy increase in the additional energy release rate (Fig. 8d). It reveals that as the abrasion loading increases, the normal load plays a more important role in contributing to the generation of particulate matter during the abrasion process.

4.3. *On the critical point of* $G_{total} = G_{critical}$

In this section, we study the conditions when the theoretically calculated total energy release rate reaches the critical energy release rate of the materials (Fig. 9). Four materials used in the experiments are selected, with the critical energy release rate (namely critical fatigue threshold shown in Fig. 4) measured as: material B 40.2 J/m^2, material C 17.24 J/m^2, material D 12.59 J /m^2, and material E 9.60 J/m^2 . According to the Eq. (85), the total energy release rate G_{total} is a function of various parameters. When the material and

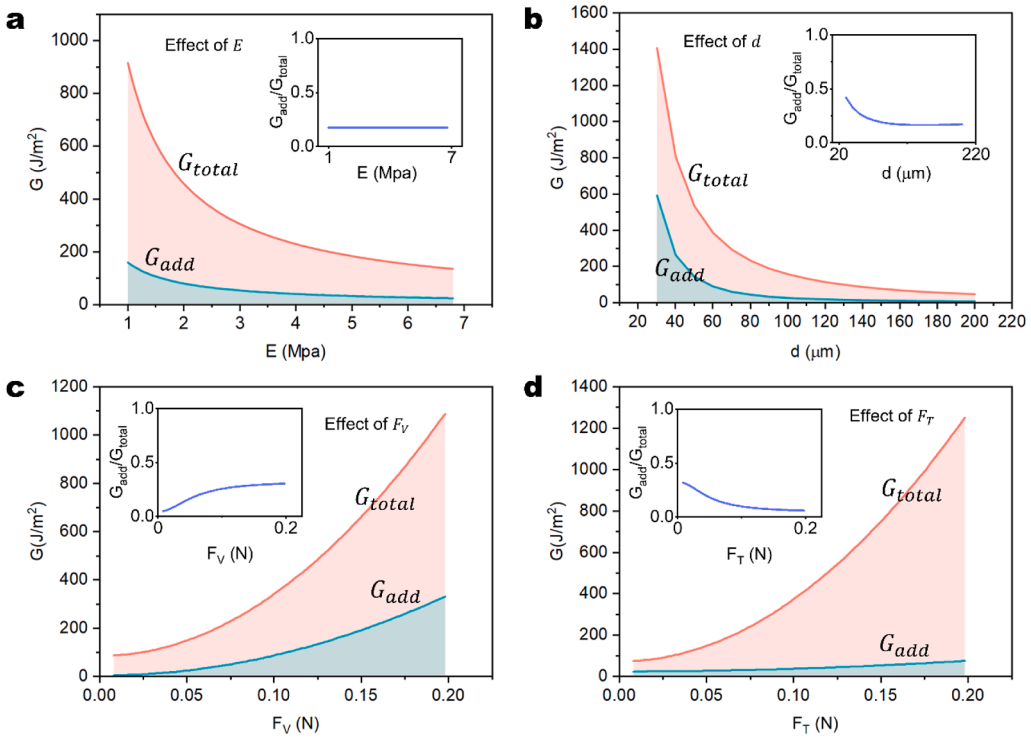

Fig. 8. Parameter study for the total energy release rate and the additional energy release rate. (A) the total energy release rate and the additional energy release rate in a function of young's modulus. (B) the total energy release rate and the additional energy release rate in a function of depth of the macro crack. (C) the total energy release rate and the additional energy release rate in a function of frictional force in the horizontal direction. (D) the total energy release rate and the additional energy release rate in a function contact force in the vertical downward direction.

sandpaper are fixed, some parameters can be determined, for example E, B, d, and L_c. Therefore, under a given loading case, G_{total} is varied with varying parameters F_V, F_T, and $\langle a \rangle$. G_{total} is considered as a 3D field function in a configuration space with the three independent variables. The 3D density plots of the total energy release rate are demonstrated with F_V on the X-axis, F_T on the Y-axis, and $\langle a \rangle$ on the Z-axis. Different colors and transparency represent the value of the G_{total}. The contour surfaces are also drawn when the total energy release rate G_{total} is equal to the critical energy release rate of the material. On the top side of this contour surface, $G_{total} < G_{critical}$, and the material tends to have a small amount of particles emissions when conducting wear experiments. While on the bottom side of the contour surface, $G_{total} > G_{critical}$, and the material tends to have great amount of particles emissions. By examining the contour surfaces of the four materials with different critical energy release rates, it becomes evident that to reach a higher critical energy release rate necessitates greater horizontal and vertical forces to be exerted on the material (Fig. 9). For example, for material B and E with the same fixed $\langle a \rangle$ as 2×10^{-7} m, the force applied on material B ($F_V \approx 0.009$ N, $F_T \approx 0.009$ N) will be much larger than the force applied on material E ($F_V \approx 0.005$ N, $F_T \approx 0.005$ N) to make the material reach the critical energy release rate.

4.4. Calibration of dispersion rate β

We next calibrate the dispersion rate β for the model framework. As shown in the problem-solving procedure in Fig. 5, we first fit the particle size probability distribution of the particulate matter emitted from Material C to a Weibull distribution to obtain two parameters λ and k (Fig. 10a). From the obtained probability density of PM10 particles, we can estimate the crack propagation rate during the abrasion process using Eq. (95). Then, we refer to the fatigue property curve of Material C shown in Fig. 4e to find out the required the energy release rate G corresponding to the estimated crack propagation rate. Next, considering Eq. (85), allowing $G = G_{total}$ can lead to the calibration of the dispersion rate β, given a proper selection of N_{total} to make sure the calculated particle concentration to agree with the experimental results shown in Fig. 10b. In this problem, we obtain $\beta = 7.92447 \times 10^{-9}$. In the following sections, we will use this dispersion rate β to calculate the density of the emitted PM10 in the air and then compared the calculated PM10 density with the corresponding experimental results.

4.5. Effect of material toughness on particulate emission

Next, we use the calibrated dispersion rate β to calculate the concentrations of particulate matter emitted by materials with various material toughness. Similar to Section 4.4, following the procedure shown in Fig. 5, we first estimate the required energy release rate G

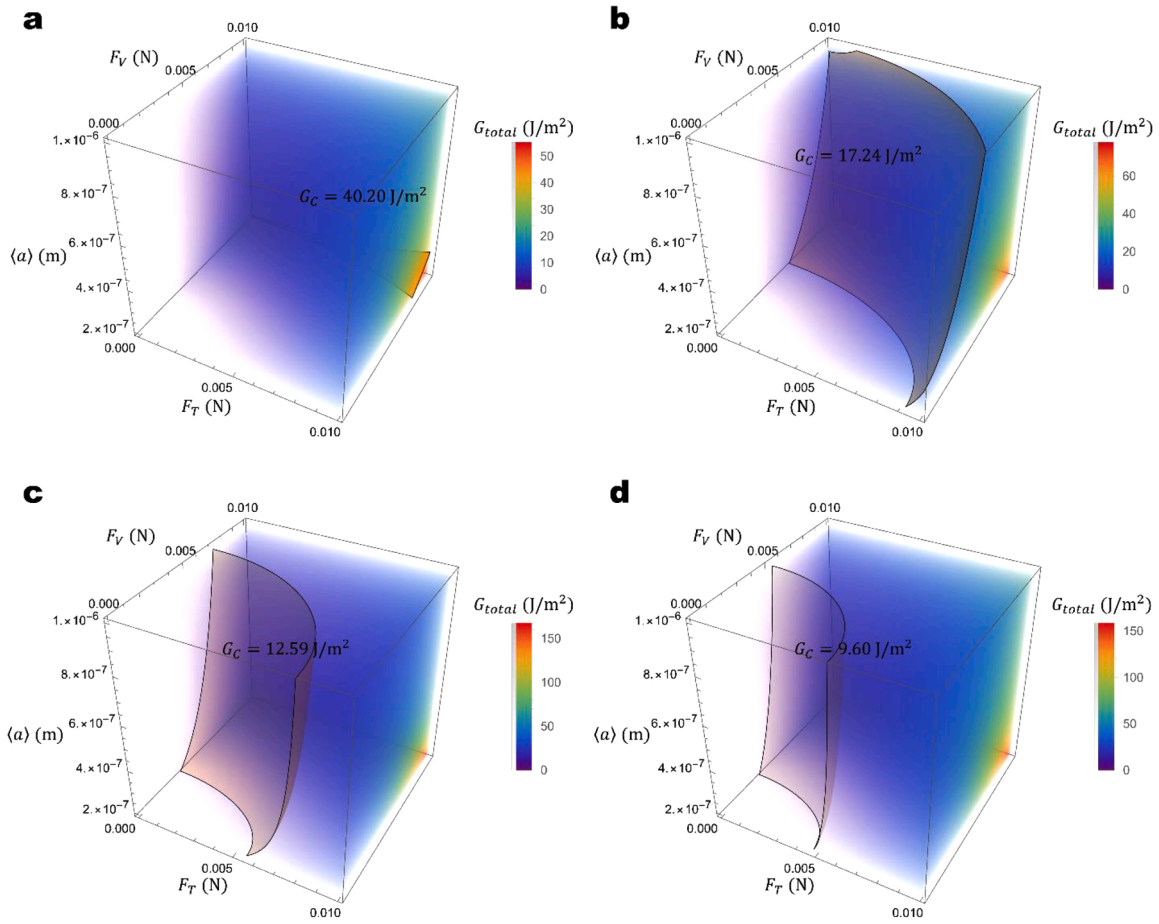

Fig. 9. Density plot of energy release rate G under various parameters F_T, F_V, and $\langle a \rangle$. Subplots (A) to (D) correspond to material B to material E. The isovalue surface represents critical energy release rate G_c.

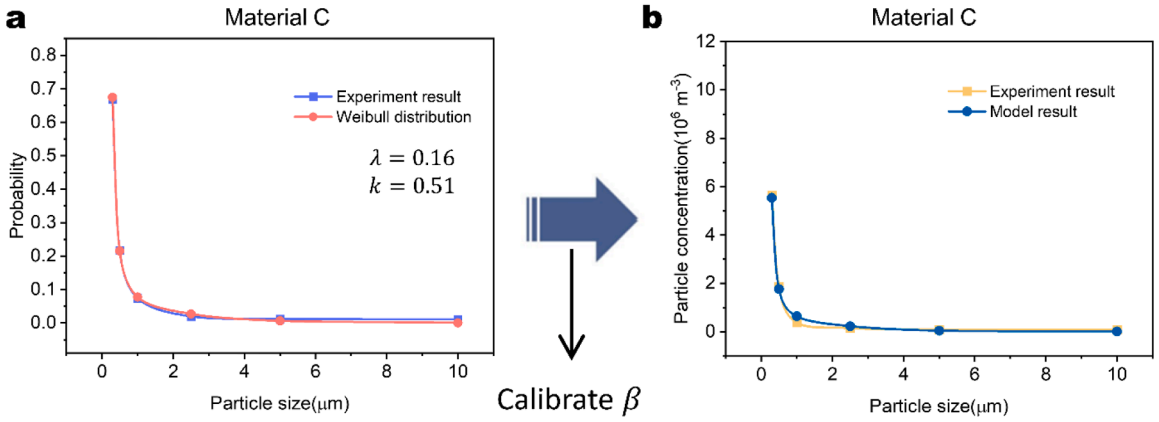

Fig. 10. Calibration of the dispersion rate with experimental results of Material C. (a) probability size distribution of the emitted particles from Material C. (b) Particle concentration of the emitted particles from Material C.

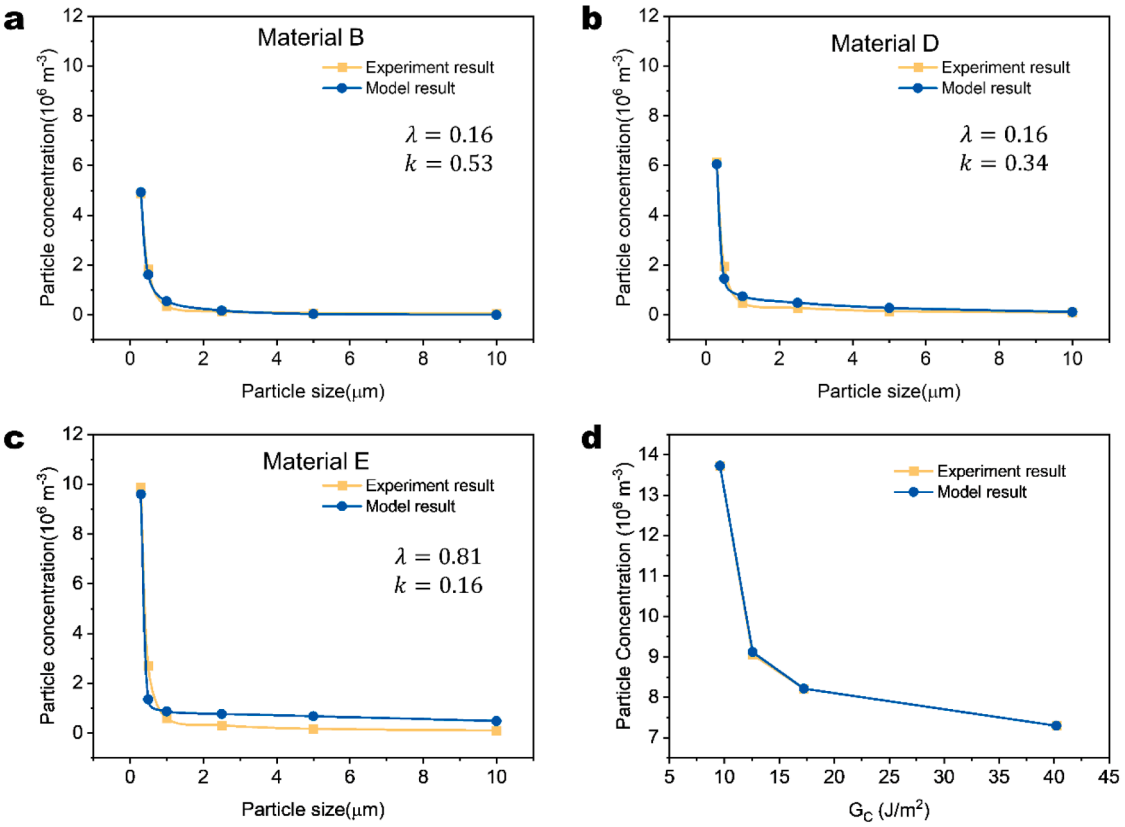

Fig. 11. Effect of material toughness on the particulate emission. Particle concentrations of PM10 particles emitted from various materials: (a) Material B, (b) Material D and (c) Material E. P150 sandpaper and compression force 3 N are employed in experiments for each case. (d) PM10 concentration as a function of the fatigue threshold toughness G_c.

from the fatigue fracture curve and then calculate the total energy release rate G_{total} from Eq. (85). Allowing $G = G_{total}$ leads to the calculation of the PM10 concentration in the air (N_{total}).

In this section, we use P150 sandpaper and normal force 3 N for compression force, and only vary the material toughness to study the effect of the material toughness on the particulate emission. The experimentally measured concentration distributions of PM10 particles emitted from five types of materials are shown in Fig. 3. We use the calibrated dispersion rate β to calculate the concentration distributions of PM10 particles emitted from Material B, D, and E are shown in Fig. 11a–c. Note that Material C has been used to calibrate β in Fig. 10. Material A is not selected to show here because the toughness of Material A is so high that the applied energy release rate is lower than the critical fatigue threshold. Ideally, Material A is not supposed to allow the crack propagation under the given loading condition, thus the measured PM10 concentration of Material A is also much lower than those of Materials B-E (Fig. 3). As shown in Figs. 11a–c, the calculated particle concentrations from the model agree with the experimentally measured particle concentrations, thus validating the proposed theoretical framework.

To summarize the effect of the material toughness on the particulate emission, we plot the PM10 concentration versus the fatigue threshold toughness G_c (Fig. 11d). Under the same loading condition, the emitted PM10 concentration increases as the material toughness decreases and the increasing becomes more rapidly as the material toughness decreases.

4.6. Effect of normal force on particulate emission

In this section, we study the effect of the normal compression forces on the particulate emission. We employ Material B and P150 sandpaper and vary the normal compression forces from 3 N to 6 N. Fig. 12a–d show both model and experimental results for the particle concentrations under normal compression forces of 3 N, 4 N, 5 N, and 6 N, respectively. The results calculated from the model agree well with the experimental results in each case. Such universal agreements demonstrate the validity of our theoretical framework again. We further summarize the PM10 concentration as a function of the normal compression force in Fig. 12e. The results reveal that the emitted PM10 concentration increases with the normal load roughly in a linear fashion. Such result further indicate that heavier vehicles may emit more PM10 particles if their tires maintain as the same and the emitted PM10 concentration may be proportional to the vehicle weight.

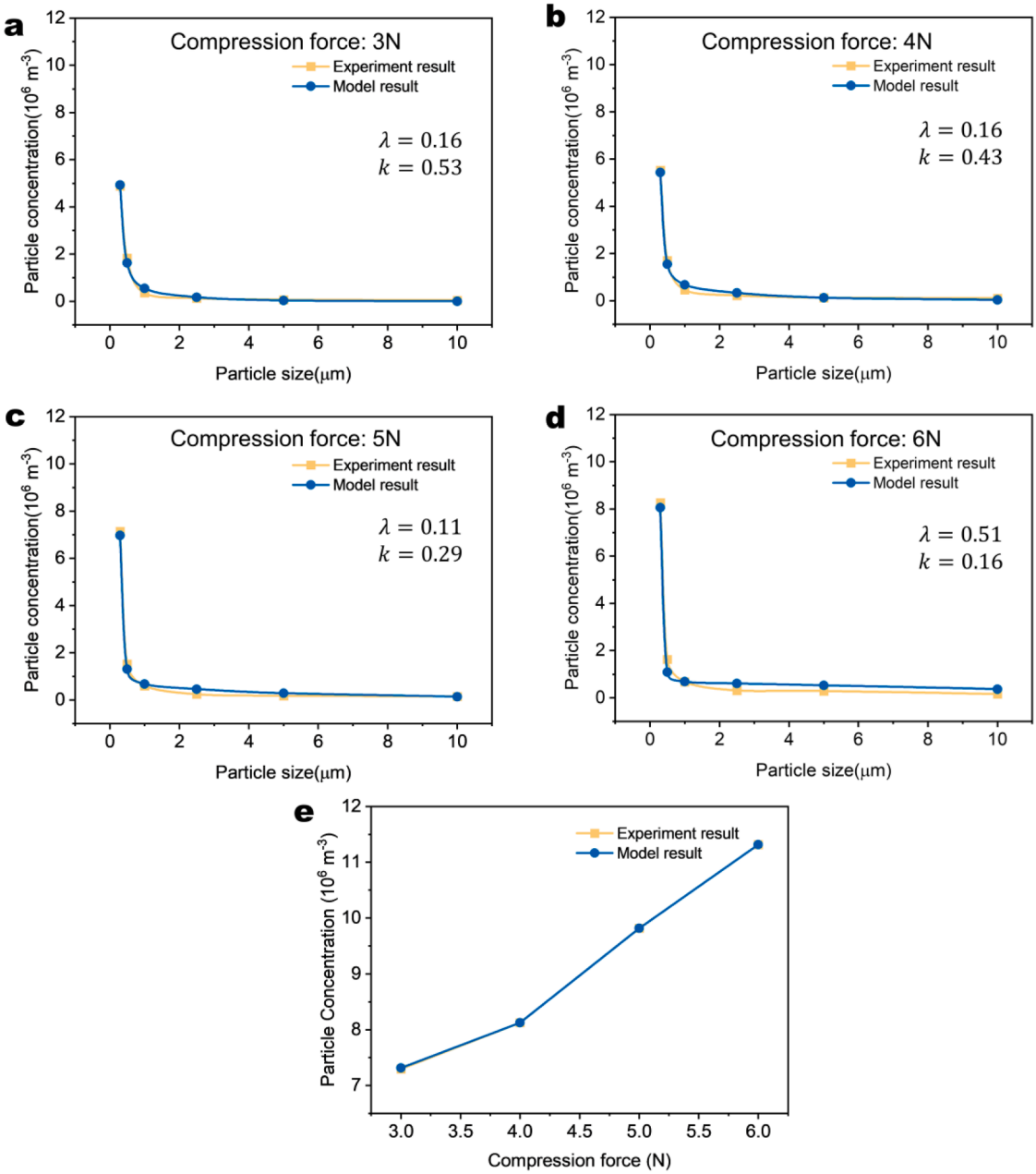

Fig. 12. Effect of normal forces on the particulate emission. Particle concentrations of PM10 particles emitted from Material B under various compression forces: (a) 3 N, (b) 4 N, (c) 5 N, and (d) 6 N. P150 sandpaper is employed in experiments for each case. (e) PM10 concentration as a function of the normal compression force.

4.5. Effect of surface roughness on particulate emission

Finally, we study the effect of the surface roughness on the particulate emission. We employ Material B and normal compression force 3 N, and vary the sandpaper types among P120, P150, P180, and P220. Fig. 13a–d shows both model and experimental results for the particle concentrations for sandpaper P120, P150, P180, and P220, respectively. Again, the model results agree well with the experimental results in each case. Scanning electron microscope images of the sandpaper surfaces reveal that the grit size of the sand decreases and the grit density increases from P120 to P220 (Fig. 13e), which is corresponding to an increase of the surface roughness. With increasing surface roughness, the emitted PM10 concentration indeed increases accordingly as shown in Fig. 13f. Our model framework can successfully calculate the PM10 concentration for each roughness case and the model result is consistent with the respective experimental result (Fig. 13f).

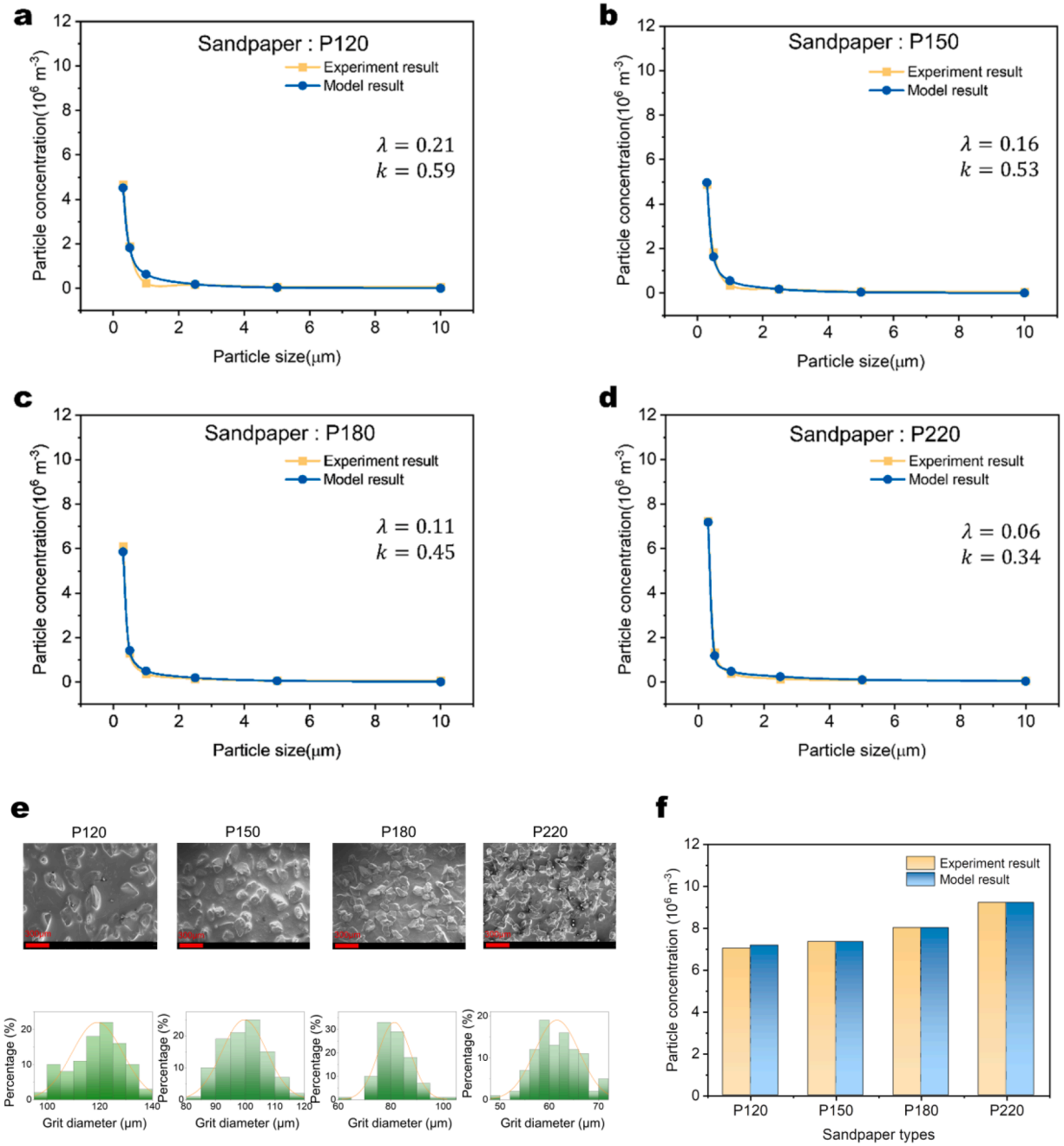

Fig. 13. Effect of surface roughness on the particulate emissions. Particle concentrations of PM10 particles emitted from Material B with various sandpapers: (a) P120, (b) P150, (c) P180, and (d) P220. (e) Scanning electron microscope images and the corresponding grit diameter distribution of the surfaces of sandpapers P120, P150, P180, and P220. (f) PM10 concentration for different sandpaper types.

5. Conclusions

This paper presents a theoretical framework for understanding the emission of particulate matter resulting from abrasion of organic materials. To elucidate the mechanisms theoretically, a multiscale model comprised of three sub-models is developed, including a macroscopic fracture model, a cracked body effective modulus model, and an additional energy release rate model. At the macroscopic level, the process of material wear and tear can be viewed as the crack propagation process of macroscopic cracks under cyclic loading. The macroscopic fracture model we developed effectively explains this process and quantitatively provides the energy release rate associated with the macro-crack. At the microscopic level, under cyclic loading, the material sustains damage due to the propagation of

numerous randomly oriented microcracks. The generation and propagation of micro-cracks within the material have two effects. Firstly, it weakens the modulus of the original material, which is explained by the cracked body effective modulus model. Secondly, the propagation of microcracks results in an additional rate of energy release, providing a reasonable explanation for the generation of finer particles emission. Our model effectively combines the macro-crack and micro-cracks and considers the additional release rate that predecessors did not account for. To validate the theory, we conducted corresponding experiments and discovered that the model and experimental results exhibit high consistency.

At the macroscopic scale, the fracture propagation results from the abrasion and scratch process, and it is described by a boundary value problem in terms of stress. The stress solution under contact loads F_V and friction load F_T is accurately solved in a form of infinite series via Beltrami's stress compatibility equation. Since the stress components in the Y direction are negligible, the Filon average is performed on the three-dimensional (3D) elastic solution, and thus we convert this 3D BVP into a plane stress/strain problem. To get the complete solution of the displacement field, two conjugate potential functions are constructed and determined by the Cauchy-Riemann equation. With the stress and displacement components established, the J integral is conducted to evaluate the strain energy release rate at the macroscopic scale. While at the microscopic scale, the damage inflicted on materials by cyclic loading can be modeled as the generation and propagation of 2D, randomly oriented microcracks within the material. We assume the energy loss generated by a single isolated microcrack in an infinite medium possesses the effective properties of a cracked body. The self-consistent procedure was subsequently described for obtaining the effective moduli of the body with micro-cracks under both plane stress and plane strain conditions. In accordance with the definition of energy release rate in fracture mechanics, we defined and calculated the additional energy release rate for microcracks. Upon comparing our results with experimental findings, we conclude that accounting for the additional energy release rate of microcracks can substantially improve the accuracy of the calculation results.

The primary contribution of this research work lies in establishing a quantitative relationship between fracture mechanics and PM10 emissions. With appropriate assumptions, this framework enables the calculation of the concentration of abrasion-induced particulate emissions. This work not only provides a comprehensive understanding of the mechanism behind the formation of particulate emissions but also has the potential to contribute to the reduction of such pollutants in the future. Being the first-generation mechanics model for abrasion-induced particulate emission, this model makes certain assumptions to simplify the calculation process. First, the linear elasticity and small deformation conditions are presumed throughout this work. Even though the polymer may endure a substantial deformation at the crack tip, the infinitesimal deformation theory with a linear constitutive model is helpful for researchers to understand the proposed cross-scale fracture mechanism, and it is at a minor sacrifice of accuracy. However, this generic concept and methodology can be extended to finite deformation theory with nonlinear constitutive models with the help of numerical methods. Second, the interaction of microcracks is not considered, which is reasonable for low microcrack density but may not be suitable for simulating the effect on material modulus at high microcrack density. Moreover, the microcracks are assumed to be randomly oriented 2D cracks that penetrate through the thickness direction. Future studies should carefully consider the 3D shape of the micro-cracks within the body.

CRediT authorship contribution statement

Ketian Li: Writing – review & editing, Writing – original draft, Visualization, Validation, Resources, Methodology, Investigation, Formal analysis, Data curation. **Yanchu Zhang:** Writing – review & editing, Visualization, Validation, Resources, Methodology, Investigation, Formal analysis, Data curation. **Kunhao Yu:** Resources, Methodology, Investigation, Formal analysis, Data curation. **Haixu Du:** Resources, Methodology, Investigation. **Constantinos Sioutas:** Writing – review & editing, Supervision, Resources, Project administration, Methodology, Investigation, Conceptualization. **Qiming Wang:** Writing – review & editing, Writing – original draft, Visualization, Supervision, Resources, Project administration, Methodology, Investigation, Funding acquisition, Formal analysis, Conceptualization.

Declaration of competing interest

The authors declare no competing financial or non-financial interests.

Data availability

Data will be made available on request.

Acknowledgments

Q.W. acknowledges the funding support from the National Science Foundation (CMMI-1943598, CMMI-2229228, and DBI-2222206) and the Office of Naval Research (N00014–22–1–2019).

References

Akono, A.T., Reis, P.M., Ulm, F.J., 2011. Scratching as a fracture process: from butter to steel. Phys. Rev. Focus 106, 204302.
Akono, A.T., Ulm, F.J., 2011. Scratch test model for the determination of fracture toughness. Eng. Fract. Mech. 78, 334–342.

Akono, A.T., Ulm, F.J., 2012. Fracture scaling relations for scratch tests of axisymmetric shape. J. Mech. Phys. Solids 60, 379–390.
Akono, A.T., Ulm, F.J., 2014. An improved technique for characterizing the fracture toughness via scratch test experiments. Wear 313, 117–124.
Andrady, A.L., 2011. Microplastics in the marine environment. Mar. Pollut. Bull. 62, 1596–1605.
Archard, J.F., 1953. Contact and rubbing of flat surfaces. J. Appl. Phys. 24, 981–988.
Austin, L.G., Klimpel, R.R., Luckie, P.T., 1984. Process Engineering of Size Reduction: Ball Milling. Society of Mining Engineers of the AIME.
Besseling, E., Wegner, A., Foekema, E.M., van den Heuvel-Greve, M.J., Koelmans, A.A., 2013. Effects of microplastic on fitness and PCB bioaccumulation by the lugworm Arenicola marina (L.). Environ. Sci. Technol. 47, 593–600.
Boerger, C.M., Lattin, G.L., Moore, S.L., Moore, C.J., 2010. Plastic ingestion by planktivorous fishes in the North Pacific Central Gyre. Mar. Pollut. Bull. 60, 2275–2278.
Browne, M.A., Crump, P., Niven, S.J., Teuten, E., Tonkin, A., Galloway, T., Thompson, R., 2011. Accumulation of microplastic on shorelines woldwide: sources and sinks. Environ. Sci. Technol. 45, 9175–9179.
Brunekreef, B., Holgate, S.T., 2002. Air pollution and health. Lancet 360, 1233–1242.
Buckeridge, D.L., Glazier, R., Harvey, B.J., Escobar, M., Amrhein, C., Frank, J.J., 2002. Effect of motor vehicle emissions on respiratory health in an urban area. Environ. Health Perspect. 110, 293–300.
Budiansky, B., O'connell, R.J.J., 1976. Elastic moduli of a cracked solid. Int. J. Solids Struct. 12, 81–97.
Cadle, S., Williams, R.J.R.C., 1979. Gas and particle emissions from automobile tires in laboratory and field studies. J. Air Pollut. Control Assoc. 52, 146–158.
Carpenter, E.J., Anderson, S.J., Harvey, G.R., Miklas, H.P., Peck, B.B.J., 1972. Polystyrene spherules in coastal waters. Science 178, 749–750.
Champ, D., Southern, E., Thomas, A.J.A., 1974. Fracture mechanics applied to rubber abrasion. Wear 133–144.
Cole, M., Lindeque, P., Fileman, E., Halsband, C., Goodhead, R., Moger, J., Galloway, T.S., 2013. Microplastic ingestion by zooplankton. Technol. Singap World Sci. 47, 6646–6655.
Cole, M., Lindeque, P., Halsband, C., Galloway, T.S.J., 2011. Microplastics as contaminants in the marine environment: a review. Mar. Pollut. Bull. 62, 2588–2597.
Evangeliou, N., Grythe, H., Klimont, Z., Heyes, C., Eckhardt, S., Lopez-Aparicio, S., Stohl, A., 2020. Atmospheric transport is a major pathway of microplastics to remote regions. Nat. Commun. 11, 3381.
Fan, Z., Meng, Q., Weisel, C., Shalat, S., Laumbach, R., Ohman-Strickland, P., Black, K., Rodriguez, M., Bonanno, L.J., 2006. Acute short-term exposures to PM2. 5 generated by vehicular emissions and cardiopulmonary effects in older adults. Epidemiology 17, S213–S214.
Garbin, H., Knopoff, L.J.Q., 1973. The compressional modulus of a material permeated by a random distribution of circular cracks. Q. Appl. Math. 30, 453–464.
Gdoutos, E.E., 2020. Fracture Mechanics: An Introduction. Springer Nature.
Grimmett, G., Stirzaker, D., 2020. Probability and Random Processes. Oxford university press.
Harrison, R.M., Jones, A.M., Gietl, J., Yin, J., Green, D.C., 2012. Estimation of the contributions of brake dust, tire wear, and resuspension to nonexhaust traffic particles derived from atmospheric measurements. Environ. Sci. Technol. 46, 6523–6529.
Hidalgo-Ruz, V., Gutow, L., Thompson, R.C., Thiel, M.J., 2012. Microplastics in the marine environment: a review of the methods used for identification and quantification. Environ. Sci. Technol. 46, 3060–3075.
Hoenig, A., 1979. Elastic moduli of a non-randomly cracked body. Int. J. Solids Struct. 15, 137–154.
Ivar do Sul, J.A., Costa, M.F., 2014. The present and future of microplastic pollution in the marine environment. Environ. Pollut. 185, 352–364.
Kampa, M., Castanas, E., 2008. Human health effects of air pollution. Environ. Pollut. 151, 362–367.
Kole, P.J., Lohr, A.J., Van Belleghem, F., Ragas, A.M.J., 2017. Wear and tear of tyres: a stealthy source of microplastics in the environment. Int. J. Environ. Res. Public Health 14.
Laws, N., Brockenbrough, J., 1987. The effect of micro-crack systems on the loss of stiffness of brittle solids. Int. J. Solids Struct. 23, 1247–1268.
Masiol, M., Hofer, A., Squizzato, S., Piazza, R., Rampazzo, G., Pavoni, B., 2012. Carcinogenic and mutagenic risk associated to airborne particle-phase polycyclic aromatic hydrocarbons: a source apportionment. Atmos. Environ. 60, 375–382.
Panko, J., Kreider, M., Unice, K., 2018. Review of tire wear emissions, Non-Exhaust Emissions, pp. 147–160.
Pant, P., Harrison, R.M.J., 2013. Estimation of the contribution of road traffic emissions to particulate matter concentrations from field measurements: a review. Atmos. Environ. 77, 78–97.
Parker-Jurd, F.N.F., Napper, I.E., Abbott, G.D., Hann, S., Thompson, R.C., 2021. Quantifying the release of tyre wear particles to the marine environment via multiple pathways. Mar. Pollut. Bull. 172, 112897.
Penkała, M., Ogrodnik, P., Rogula-Kozłowska, W.J., 2018. Particulate matter from the road surface abrasion as a problem of non-exhaust emission control. Environments 5, 9.
Rosin, P.J.J., 1933. Laws governing the fineness of powdered coal. 7, 29–36.
Sommer, F., Dietze, V., Baum, A., Sauer, J., Gilge, S., Maschowski, C., Gieré, R., 2018. Tire abrasion as a major source of microplastics in the environment. Aerosol. Air. Qual. Res. 18, 2014–2028.
Suh, N.P.J., 1973. The delamination theory of wear. Wear 25, 111–124.
Sun, L., Ju, J.J., 2004. Elastoplastic modeling of metal matrix composites containing randomly located and oriented spheroidal particles. J. Appl. Mech. 71, 774–785.
Thorpe, A., Harrison, R.M.J., 2008. Sources and properties of non-exhaust particulate matter from road traffic: a review. Sci. Total Environ. 400, 270–282.
Tonegawa, Y., Sasaki, S., 2021. Development of tire-wear particle emission measurements for passenger vehicles. Emission Control Sci. Technol. 7, 56–62.
Wagner, S., Huffer, T., Klockner, P., Wehrhahn, M., Hofmann, T., Reemtsma, T., 2018. Tire wear particles in the aquatic environment - a review on generation, analysis, occurrence, fate and effects. Water Res. 139, 83–100.